INL/EXT-17-41852
Revision 1

Light Water Reactor Sustainability Program

Interrogation of Alkali-Silica Reaction Degraded Concrete Samples using Acoustic and Thermal Techniques to Support Development of a Structural Health Monitoring Framework

April 2017

U.S. Department of Energy
Office of Nuclear Energy

INL/EXT-17-41852
Revision 1

Light Water Reactor Sustainability Program

Interrogation of Alkali-Silica Reaction Degraded Concrete Samples using Acoustic and Thermal Techniques to Support Development of a Structural Health Monitoring Framework

Sankaran Mahadevan
Sarah Miele
Kyle Neal
Yanqing Bao
Vivek Agarwal
Binh T. Pham
Douglas Adams

April 2017

Idaho National Laboratory
Idaho Falls, Idaho 83415

Vanderbilt University
Nashville, Tennessee 37235

Prepared for the
U.S. Department of Energy
Office of Nuclear Energy
Under DOE Idaho Operations Office
Contract DE-AC07-05ID14517

ABSTRACT

Assessment and management of aging concrete structures in nuclear power plants require a more systematic approach than simple reliance on existing code margins of safety. Health monitoring of concrete structures is performed to understand the current condition of a structure based on heterogeneous measurements and then produce high-confidence actionable information regarding structural integrity. This information can then be used to support operational and maintenance decisions. The proposed diagnosis and prognosis framework consists of four elements: health monitoring, data analytics, uncertainty quantification, and prognosis.

The objectives of this ongoing research project focuses on health monitoring and data analytics of concrete slab cast, which is cured using four pockets of reactive aggregates: pure silica, wells, placitas, and spratt. A controlled concrete slab with four aggregates is cast at Vanderbilt University in representative conditions to accelerate degradation due to alkali-silica reaction (ASR). Four nondestructive evaluation (NDE) techniques (thermography, mechanical deformation measurements, nonlinear impact resonance-acoustic spectroscopy, and vibro-acoustic modulation) are used to examine the degraded concrete slab. Heterogeneous data from these techniques are analyzed for assessing ASR-related degradation in concrete samples. In addition, this report discusses thermography assessment of three cement bricks cured under different conditions to accelerate ASR-related degradation. The application of the digital image correlation technique to study ASR-related degradation on a large concrete sample at the University of Tennessee Knoxville is discussed and initial observations are presented in this report.

The results from the data analysis of the NDE techniques on concrete slab cured at Vanderbilt University are discussed in detail in this report. The major outcome of the analysis suggests that the nonlinear impact resonance acoustic spectroscopy is able to detect potential degradation in a concrete slab but is unable to locate or isolate the degradation. Alternatively, the vibro-acoustic technique is able to detect degradation and locate the damage in the concrete slab cast. The outcomes supports development of a structural health monitoring framework.

EXECUTIVE SUMMARY

One challenge facing the current fleet of light water reactors in the United States is age-related degradation of their passive assets, including concrete, cables, piping, and the reactor pressure vessel. As the current fleet of nuclear power plants (NPPs) continues to operate for 60 years or more, it is important to understand the current and the future condition of passive assets under different operating conditions that would support operational and maintenance decisions. To ensure safe and reliable long-term operation of the current fleet, the U.S. Department of Energy's Office of Nuclear Energy funds the Light Water Reactor Sustainability Program to develop the scientific basis for extending the operation of commercial light water reactors beyond the current license extension period.

Among the different passive assets of interest in NPPs, concrete structures are investigated in this research project. Reinforced-concrete structures found in NPPs can be grouped into following categories: (1) primary containment, (2) containment internal structures, (3) secondary containments/reactor buildings, and (4) spent fuel pool and cooling towers. These concrete structures are affected by a variety of degradation mechanisms that are related to chemical, physical, and mechanical causes and to irradiation. Age-related degradation of concrete results in gradual microstructural changes (e.g., slow hydration, crystallization of amorphous constituents, and reactions between cement paste and aggregates). The purpose of structural health monitoring of concrete is to assess the current condition of a structure and to provide high-confidence actionable information regarding structural integrity and reliability. Vanderbilt University, in collaboration with Idaho National Laboratory and Oak Ridge National Laboratory, is developing a probabilistic framework for structural health monitoring and managing the condition of aging concrete structures in NPPs. This integrated framework includes four elements: (1) monitoring, (2) data analytics, (3) uncertainty quantification, and (4) prognosis.

The objective of this continuing research project is to obtain degradation data for concrete structures from a series of experiments conducted under controlled laboratory conditions. The ability of nondestructive examination (NDE) methods to characterize concrete deterioration and correlate it with structural performance is also being assessed. This report focuses on concrete degradation caused by alkali-silica reaction (ASR). Concrete specimens were prepared to develop accelerated ASR degradation in a laboratory setting. NDE techniques, which include thermography, mechanical deformation measurements, nonlinear impact resonance-acoustic spectroscopy, and vibro-acoustic modulation, are used to detect the damage caused by ASR on concrete slabs cured at Vanderbilt University. Heterogeneous data from the four NDE techniques are used for assessing the damage to the concrete slab in the presence of four pockets of reactive aggregates. The measured data can be linked to a probabilistic framework; the monitoring data were input to a Bayesian network for information fusion, uncertainty quantification of a diagnosis result, and prognosis to facilitate implementation of continuous online monitoring of realistic NPP structures.

Some of the outcomes of these experiments are as follows:

1. A 24 × 24 × 6 in. concrete slab was cast at Vanderbilt University with four different types of reactive aggregate and aggressively cured to produce accelerated ASR degradation.
2. The impacts of ASR development on the test specimen were examined using four non-destructive evaluation techniques: thermography, mechanical deformation measurement, nonlinear impact resonance-acoustic spectroscopy, and vibro-acoustic modulation.
3. Nonlinear impact resonance acoustic spectroscopy is able to detect potential degradation in a concrete slab, but it is unable to locate or isolate the degradation. The vibro-acoustic technique on the other hand, is able to detect degradation and locate the damage in the concrete slab cast at Vanderbilt University.

4. Thermography assessment of bricks, cured under different conditions to accelerate ASR-related degradation is discussed.
5. The digital image correlation is an ongoing study of a large concrete specimen constructed at University of Tennessee, Knoxville. The researchers have collected four sets of data tracking the deformation of the specimen due to ASR.

The experiments described in this milestone report are focused on concrete structural monitoring measurements and data analytics. This will support continuous assessment of concrete performance and enhancing the structural health framework.

During the next phase of research, the vibro-acoustic technique will be further studied for detection and localization of ASR in a reinforced-concrete slab and concrete slabs cured at University of Alabama with different reactive aggregates. The uncertainty quantification approaches and integration framework will be advanced further to handle large amounts of observation data. The resulting comprehensive approach will facilitate development of a quantitative, risk-informed framework that would be generalizable for a variety of concrete structures.

ACKNOWLEDGMENTS

This report was made possible through funding by the U.S. Department of Energy's Light Water Reactor Sustainability Program. We are grateful to Richard Reister of the U.S. Department of Energy and Bruce Hallbert and John C. Wagner at Idaho National Laboratory for championing this effort. We also thank Jodi Vollmer and Heather M. Rohrbaugh at Idaho National Laboratory for technical editing and formatting of the report.

CONTENTS

FIGURES

TABLES

ACRONYMS

ASR	alkali-silica reaction
DIC	digital image correlation
EPRI	Electric Power Research Institute
ICP-OES	Inductively Coupled Plasma-Optical Emission Spectroscopy
NaOH	sodium hydroxide
NDE	nondestructive examination
NIRAS	nonlinear impact resonance-acoustic spectroscopy
NPP	nuclear power plant
PSD	power spectral density
SHM	structural health monitoring
VAM	vibro-acoustic modulation

Interrogation of Alkali-Silica Reaction Degraded Concrete Samples using Acoustic and Thermal Techniques to Support Development of a Structural Health Monitoring Framework

1. INTRODUCTION

The majority of existing nuclear power plants (NPPs) continues to operate beyond their initial licensed life expectancy. The passive structures, systems, and components of NPPs as they continue to operate suffer deterioration that affects structural integrity and performance. Monitoring the condition of these elements of an NPP is essential for ensuring that their conditions meet performance and safety requirements over the entire expected plant lifespan. This project focuses on concrete structures in NPPs. The concrete structures are grouped into the following categories: (1) primary containment, (2) containment internal structures, (3) secondary containment/reactor buildings, and (4) other structures such as used fuel pools, dry storage casks, and cooling towers. These concrete structures are affected by a variety of chemical, physical, and mechanical degradation mechanisms, such as alkali-silica reaction (ASR), chloride penetration, sulfate attack, carbonation, freeze-thaw cycles, shrinkage, and mechanical loading (Naus 2007). The age-related deterioration of concrete results in continuing microstructural changes (e.g., slow hydration, crystallization of amorphous constituents, and reactions between cement paste and aggregates). Therefore, it is important that changes over long periods of time are measured and monitored, and that their impacts on the integrity of the components are analyzed to best support long-term operations and maintenance decisions of existing fleet of nuclear reactors.

Structural health monitoring (SHM) can produce actionable information regarding structural integrity that, when conveyed to the decision-maker, enables risk management with respect to structural integrity and performance. The SHM methods and technologies include assessment of critical measurements, monitoring, and analysis of aging concrete structures under different operating conditions. In addition to data from the specific system being monitored, information may also be available for similar or nominally identical systems in an operational NPP fleet, as well as legacy systems. Therefore, to take advantage of this valuable information Christensen (1990) suggested that assessment and management of aging concrete structures in NPPs requires a more systematic and dynamic approach than simple reliance on existing code margins of safety.

Through the Light Water Reactor Sustainability Program, national laboratories (Idaho National Laboratory and Oak Ridge National Laboratory) and universities (Vanderbilt University, University of Nebraska-Lincoln, Univeresity of Alabama, University of South Carolina, and Georgia Tech University) have begun research on concrete SHM. In this report, the focus is now the joint collaboration between national laboratories and Vanderbilt University in researching concrete SHM in accordance with the proposed framework discussed in Mahadevan et al. (2014). The goal of this research is to enable plant operators to make risk-informed decisions on structural integrity, remaining useful life, and performance of concrete structures across the NPP fleet. The project long-term research objective is to produce actionable information regarding structural integrity that is individualized for a structure of interest and its performance goals. In addition, the project supports the research objectives of three pathways under the Light Water Reactor Sustainability Program (i.e., the Advanced Information, Instrumentation, and Control Systems Technologies Pathway; the Materials Aging and Degradation Pathway; and the Risk-Informed Safety Margin Characterization Pathway).

Vanderbilt University, in collaboration with Idaho National Laboratory and Oak Ridge National Laboratory, is developing a framework for evaluating and forecasting the health of aging NPP concrete structures that are subject to physical, chemical, and mechanical degradation (Mahadevan et al. 2014;

Agarwal and Mahadevan 2014). The framework will investigate concrete structure degradation by integrating the following technical elements: (1) health condition monitoring, (2) data analytics, (3) uncertainty quantification, and (4) prognosis. For details on each element of the proposed framework, refer to Mahadevan et al. (2014). The framework will help plant operators to make risk-informed decisions on structural integrity, remaining useful life, and concrete structure performance. The demonstration performed at Vanderbilt University using various techniques to assess ASR degradation in controlled concrete specimens was reported in Mahadevan et al. (2016).

The objective of this report is to examine the use of nondestructive examination (NDE) techniques in detecting ASR-related degradation in concrete specimens. These techniques include infrared (IR) thermography, digital image correlation, mechanical deformation measurement, nonlinear impact resonance-acoustic spectroscopy, and vibro-acoustic modulation. A series of experiments is been conducted at the Vanderbilt University to provide sufficient degradation data in support of the SHM framework (Mahadevan et al. 2014; Mahadevan et al. 2016) used to examine and forecast the condition of aging concrete structures in NPPs. Within this experimental campaign, multiple concrete samples are casted and exposed to different accelerated aging conditions in a laboratory to ensure formation of ASR gel within an observable time frame. These concrete samples also differ in sizes and types of embedded aggregates. The above-mentioned NDE techniques are used to detect and assess the ASR presence in these concrete samples for extended period of time. The obtained degradation data are crucial for studying impacts of operating conditions (e.g., moisture presence, sodium hydroxide [NaOH] presence, high temperature) and of aggregates embedded in concrete structures on ASR gel formation. More importantly, these degradation data can be correlated with corresponding changes in physical strength of concrete structures. Thus, the resulting functional relationships can be used within the SHM framework to predict health conditions of similar structures.

The technical background, experimental setting, data processing, significant results, technical findings, and conclusion are included in the remainder of the report is organized as follows:

- Section 2 discusses the technical basics of the ASR development and NDE techniques used to assess the effects of ASR on the integrity of concrete samples developed at Vanderbilt University.
- Section 3 describes the preparation of multiple concrete specimens exposed to different ASR accelerated degradation conditions and the laboratory experimental setup of NDE techniques.
- Data analysis methods applied to the collected monitoring data and significant technical findings are presented in Section 4.
- Research summary and future activity are discussed in Section 5.

2. TECHNICAL BACKGROUND

2.1 Development and Impact of Alkali-Silica Reaction

The ASR is a reaction in concrete between the alkali hydroxides (K^+ and Na^+) in the pore solution and the reactive non-crystalline (amorphous) silica (S^{2+}) found in many common aggregates, given sufficient moisture. This reaction occurs over time and causes the expansion of the altered aggregate by the formation of a swelling gel of calcium silicate hydrate (C-S-H). Reactive silica is mainly provided by reactive aggregates and the alkalis by the cement clinker. ASR swelling results from the relative volume increase between the product and reactant phases involved in the chemical reaction. First, the products expand in pores and micro-cracks of the cementitious matrix. Once this free expansion space is filled, the swelling is restrained, and the product phases exert local pressure on the surrounding concrete skeleton (Ulm 2000). Figure 1 depicts the mechanism of ASR (Kreitman 2011).

With water presence, the ASR gel increases in volume and exerts an expansive pressure inside the material, causing spalling micro-to macro-cracks (due to nonhomogeneous swelling related to non-uniform

moisture distribution). As a result, ASR reduces the stiffness and tensile strength of concrete, because these properties are particularly sensitive to micro-cracking. ASR also can cause serious cracking in concrete, resulting in critical structural problems that can even force the demolition of a particular structure. The serviceability of concrete structures includes the resistance to excessive deflections, as well as a host of other durability concerns that can shorten the service life of a structure. Large surface crack widths and deep penetration of open surface cracks promote ingress moisture and any dissolved aggressive agents, such as chlorides. Additionally, the loss of concrete stiffness and potential for reinforcement yield are concerns for concrete deflection capabilities.

ASR is a complex chemical phenomenon, the rate and extent of which depend on a number of material and environmental parameters, for which the interactions among parameters is not fully understood. This critical nature of ASR on premature concrete deterioration requires the quantitative assessment of ASR structural effects during service life (both in time and space). In particular, a combined experimental modeling investigation method is required to evaluate the impact of ASR on the dimensional stability of concrete structures. Although ASR has been identified as a cause of deterioration of numerous concrete structures and research has yielded some understanding of the mechanism of the reaction, the structural effects of ASR and how to best assess the extent of damage to existing structures remain major topics of ongoing research. This is because the expansion and cracking patterns (the most obvious sign of distress) caused by ASR affect both the concrete and the reinforcing steel, but similar crack patterns can also be produced by other distress mechanisms (i.e., drying shrinkage and sulfate attack).

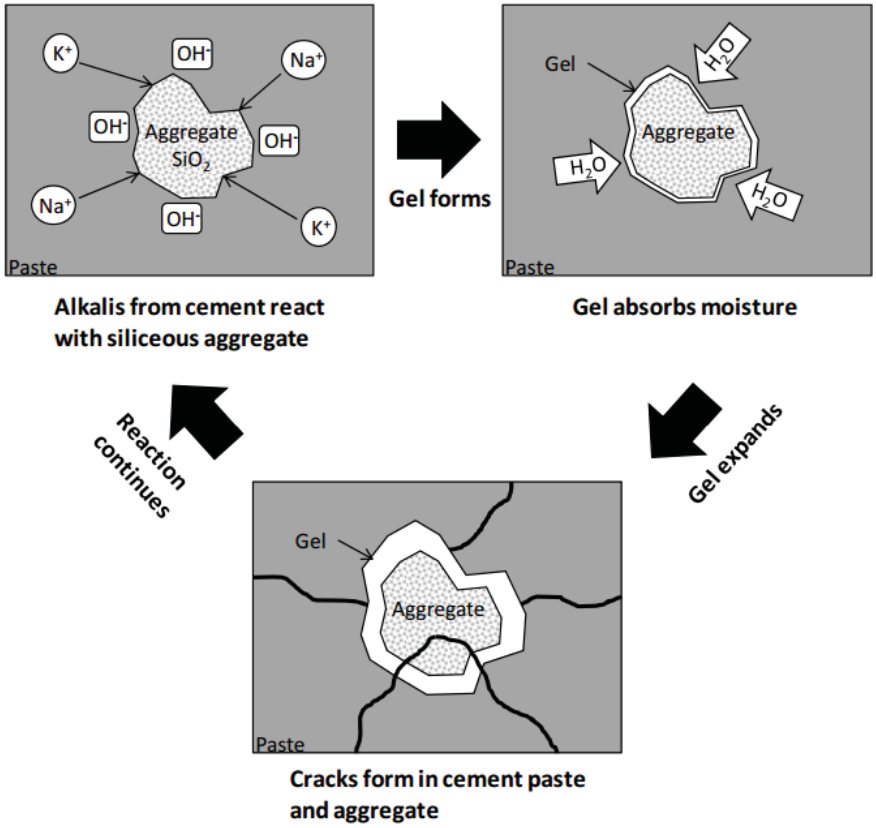

Figure 1. Mechanism of ASR (Kreitman 2011).

In the nuclear industry, a scoping study of ASR in concrete is performed to support future activities that include evaluating the effects of ASR on the structural capacity. From a safety perspective, the remaining capacity of a structure exhibiting distress due to ASR is an important factor in operational and maintenance management decisions. This is a challenging task for various reasons. First, the extent of the

degradation will vary throughout the element as a function of the moisture content and as a function of the degree of restraint provided by the steel reinforcement. Also, it may be difficult to predict the properties of the concrete using certain testing results taken from the structure, because the size of the defects caused by the ASR may be large compared to a small structure, such as the cylinder (resulting in anomalously low tested strength), but the defects are small compared to the larger structure (suggesting there may be sufficient capacity). In addition, there is no reliable nondestructive means of estimating the degree of the reaction in an existing concrete structure.

ASR can potentially affect concrete properties and performance characteristics, such as compressive strength, the modulus of elasticity, flexural stiffness, shear strength, and tensile strength (Agarwal et al 2015). ASR can also impact material properties, but the structural performance of concrete elements depends on whether or not the concrete is unconfined or confined within reinforcing bars. The concrete core testing was conducted at the Seabrook Station Nuclear Power Plant in February 2011 as part of the license renewal submission (NextEra Energy Seabrook 2012). These tests confirmed the presence of ASR-induced cracks in various structures within the plant and reduced modulus to some extent. The impact of reduced modulus on ASR-affected structures was evaluated. This evaluation found that the overall structure integrity was still within the strength requirements.

2.2 Nondestructive Evaluation Techniques for Monitoring Alkali-Silica Reaction

NDE techniques are essential for assessing ASR development in in-service concrete structures, such as those in NPPs. For monitoring the ASR progression, the optical, thermal, and acoustic techniques are used for full-field imaging. Examples of these techniques include digital image correlation (DIC), IR imaging, nonlinear impact resonance-acoustic spectroscopy, and vibro-acoustic modulation. A particular consideration is the correlation between chemical degradation mechanisms and the observed degradation, which can be used to synergy between monitoring and prognosis. The standard test methods for determining the potential alkali-silica reactivity and for determination of the amount of time needed for concrete to change due to ASR are documented in ASTM C1567-13 and ASTM C1293-08b, respectively.

2.2.1 Infrared Thermography

Infrared thermography maps the thermal load path in a material. Cracking, spalling, and delamination in concrete would create a discontinuity in the thermal load path. Additionally, rebar and tensioning cables can be easily singled out due to the difference in thermal conductivity coefficients between steel and concrete. Thermography has even been shown to detect debonding between the reinforcing steel and concrete. Infrared thermography can be either an active or passive monitoring technique. When heat is locally added to the structure to create a temperature gradient, the thermography is referred to as active. When only solar heat is used to provide heat to produce the temperature gradient, the thermography is considered passive. Passive infrared thermography is preferred, because it is less energy intensive. For small-sized concrete slabs, the active infrared thermography can be used because an additional energy source increases a thermal contrast between the concrete samples and the background.

The Electric Power Research Institute (EPRI) showed the feasibility of IR thermography by mapping a 450,000-ft^2 dam. During the 2 days that the EPRI spent mapping the dam, numerous potential delamination sites were identified (Renshaw et al. 2014). Kobayashi and Banthia (2011) combined induction heating with IR thermography to detect corrosion in reinforced concrete. Induction heating uses electromagnetic induction to produce an increase in temperature in the rebar. When corrosion is present, it inhibits the diffusion of heat from the rebar to the surrounding concrete. Infrared thermography is then used to capture the temperature gradient. It was concluded that the temperature rise in corroded rebar is higher than in non-corroded rebar. A more-corroded rebar yields a smaller temperature rise on the surface, and the technique is more effective with larger bar diameters and smaller cover depths

(Kobayashi and Banthia 2011). The current study is investigating the performance of IR thermography as a means of identifying ASR growth in concrete samples.

2.2.2 Digital Image Correlation

Digital image correlation is an optical NDE technique that is capable of measuring the deformation, displacement, and strain of a structure (Bruck et al. 2012). During the NPP routine pressure tests on containment vessels, when the internal pressure reaches 60 psi, it might be possible to use DIC to determine deformation of the concrete containment. DIC is capable of detecting surface defects, such as cracks, micro-cracks, and spalling, but it is unable to detect any subsurface defects. The primary benefit of DIC is in measuring deformation; therefore, the ability of DIC to detect changes in the dimensions of the slab due to ASR gel expansion is of interest in this study. DIC requires a speckled pattern on the specimen to anchor observations at different points in time. This also presents a problem for the cement brick specimens that are immersed in NaOH solution or water; the pattern is disturbed and partly dissolved in the NaOH solution. However, if the cement brick specimen is cured above water, DIC might be applicable.

2.2.3 Mechanical Deformation Measurement

The mechanical deformation measurement is a contact measurement technique. Calipers or an extensometer can be used to measure deformation along a linear distance. It is often convenient to glue on targets or cast nails into the concrete to provide more repeatable measurement points. To capture the ASR-induced concrete deformation, the measurement device needs to be accurate to within a few hundred microns. Most high-resolution mechanical measurement devices have a relatively short measuring span (i.e., 1 ft or less). This makes them ideal for laboratory experiments but limits their applicability in real-world structures without using a significant number of targets glued to the structure.

2.2.4 Nonlinear Impact Resonance-Acoustic Spectroscopy

All solids have natural periods of vibration, also known as resonant frequencies, at which solids tend to vibrate when excited. This is a function of the dimensions, stiffness, density, and boundary conditions (external restraint) of the solid. If two objects that have different stiffness, but are otherwise identical, are compared, the stiffer object will have a higher resonant frequency (shorter natural period). ASR and delayed ettringite formation reduce concrete's stiffness, which can be detected by measuring the resonant frequency. Linear test methods have proven reasonably effective for locating larger defects, but test methods based on nonlinear behavior may be many times more sensitive to micro-cracks and distributed damage characteristics of ASR.

Nonlinear impact resonance-acoustic spectroscopy (NIRAS) is an NDE technique that uses the vibrational response of a structure to classify damage. NIRAS was developed at Georgia Tech to detect ASR-induced damage in concrete (Lesnicki et al. 2012, Lesnicki et al. 2014). NIRAS operates based on the following idea: a linear system has the same natural frequency regardless of the amplitude of the excitation force; in contrast, for nonlinear systems, the resonant frequency experiences a downward shift as the force of the impacts increases; this shift is increasingly prominent in specimens with micro-cracking.

The nonlinearity parameter is commonly used to quantify the severity of damage. The nonlinearity parameter is calculated as a scaled slope of the input force amplitude versus the frequency shift. It is well known that concrete samples with more severe damage generally have a larger value for the nonlinearity parameter (steeper slope). On the other hand, a sample in pristine condition (or linear structure) should have no frequency shift with increasing input force amplitude, and its nonlinearity parameter would be 0.

Because ASR causes micro-cracking within the concrete, which creates nonlinearity, it is believed that NIRAS can be used to detect damage in concrete before the cracking is visible on the surface. Because NIRAS is a global vibrational response technique (i.e., it measures shifts in resonant frequency),

it is better suited for small laboratory concrete specimens than large concrete structures. For example, if a large concrete structure had a small patch of ASR growth, it is unlikely that NIRAS would be able to detect the growth, because it will have a minimal effect on the natural frequency of the structure.

2.2.5 Vibro-Acoustic Modulation

Vibro-acoustic modulation (VAM) is a nonlinear vibration technique in which the structure of interest is excited using a combination of specific frequencies and the response is recorded. VAM is also known by other names, such as nonlinear wave modulation spectroscopy. The VAM technique assumes that an undamaged structure can be represented by a linear system while the representation of a damaged structure must include nonlinearity. VAM is a NDE technique that has been successful in detecting nonlinearities in various materials, including detecting ASR-induced damage in concrete (Chen et al. 2008; Chen et al. 2009).

VAM works by exciting a structure with two frequencies of vibration simultaneously. The low-frequency input is termed the "pump," and the high-frequency input is termed the "probe" (Kim et al. 2014). Interaction of the pumping and probing signals can help identify the presence of nonlinearities in the system. As the pumping signal causes the crack to open and close, the effective cross-sectional area that the probing signal can travel through also changes. Several potential damage indices based on the response spectrum properties were considered, as follows:

- Ratio of sideband amplitude to probe signal amplitude or ratio of sideband amplitude to pump signal amplitude
- Ratio of sideband bandwidth to power of probe signal or ratio of sideband bandwidth to power of pumping signal
- Percent of total power present in sideband power.

It is worth noting that the fundamental understanding of the physics behind the nonlinear vibration phenomenon in solids is not well understood. Also, various nonlinear mechanisms exist in solids and typically are characterized as either elastic or dissipative. Compounding contributions from each of the different mechanisms may be difficult to separate. For example, compounding nonlinear effects from surface-to-surface bonding and other tangible interfaces could mask sidebands indicative of ASR-induced damage. Sideband amplitude has been known to be heavily dependent on the system excitation and boundary conditions. In addition, sideband amplitude was observed decreasing as fatigue cracks grew well past initiation. This observation could potentially be explained by the increasing dominance of global stiffness reductions as cracks grow to large lengths as compared to the significance of breathing cracks at smaller crack lengths.

In general, the influence of structural configuration, excitation voltage, boundary conditions, and crack geometry should be thoroughly addressed before fielding SHM applications using nonlinear acoustics. Thus, the VAM technique is more suitable for damage detection than for assessing the extent of the damage (Vehorn 2013).

3. CONCRETE SAMPLE

This research investigates the monitoring of degradation in concrete samples due to ASR via NDE techniques discussed in Section 2.2. Effective combinations of NDE techniques need to be identified for different types of concrete structures under different loading and operating conditions. The monitoring techniques are studied with concrete samples constructed and cured in the laboratory (a medium-sized concrete slab at Vanderbilt University and a large concrete slab at the University of Tennessee – Knoxville).

3.1 Sample Preparation and Curing

Several concrete samples were casted in the laboratory at Vanderbilt University for this study. In Mahadevan et al. 2016, cement bricks (9 × 5 × 2-in. dimension) have been cast with different aggregate types and quantities. However, one medium-sized concrete slab with dimensions of 2 ft × 2 ft × 6 in. was casted for studying of ASR in more real-world structures, which more accurately imitate what is seen at NPPs. Handling a medium-sized slab of this size is challenging in all activities including casting, curing, nondestructive testing, moving from the casting location to testing facility, and detecting ASR.

Under normal condition, the ASR is a slow-developing process that can take several decades to become visible and result in failure. In the laboratory, aggressive conditions are applied to accelerate this process so the degradation progression and corresponding data can be observable. There are several methods are used to accelerate ASR formation in concrete samples during the curing period, which allows the measureable ASR gel to be produced in the laboratory environment, leading to cracks in concrete in as soon as several months. The ASR acceleration measures are:

- *Increase humidity*. Water serves as the solvent for the silica dissolution and as transport media for the diffusion of alkali hydroxide ions through the pore solution to reaction sites. Water is also a necessary compound for formation of the various reaction products (gels, precipitates, crystals, etc.). As a result, an increase in water content in concrete affects both kinetics and magnitude of ASR gel formation.
- *Sodium hydroxide (NaOH) solution*. NaOH solution provides a rich source of alkali hydroxide ions (Na^+) in concrete pore solution, which are essential for inducing ASR. These alkalis from external sources can contribute significantly to the concrete alkali content. Thus, external alkalis may increase expansion from ASR, especially when concrete is cracked or is highly permeable.
- *Highly reactive siliceous aggregates*. Reactivity is a function of the type and form of constituents composing the aggregate. These aggregates used for this study provide rich source of reactive silica, which is an important ingredient for ASR formation. Glass is an example of highly reactive siliceous aggregates because it is basically silica. Also, different types of aggregates were inserted in the slab samples to study their impact on ASR formation.
- *High temperature*. Since ASR mechanisms are thermo-activated; the high temperature curing condition promotes the occurrence of ASRs. In addition, this high-curing temperature (>70°C) also promotes the formation of the internal sulfate attack, which leads to more damage in concrete. The effect of high temperatures on ultimate expansion is aggregate dependent with most aggregates reacting more at higher temperatures.

3.1.1 Cement Bricks

Casting Process

Two sets, each has three cement bricks were cast with 9 in. × 5 in. × 2 in. dimensions (labeled as [A1, B1, C1] and [A2, B2, C2]). The water-to-cement ratio of 0.4 was used for casting these bricks to achieve adequate workability in cement paste. The bricks were placed in the molds for 24 hours before putting in the corresponding curing location. For accelerating the ASR gel formation, thin glass sheet(s), which contains approximately 75% silicon dioxide (SiO_2), was inserted as aggregates into bricks, [B1, B2] and [C1, C2]. One large glass was inserted in each of bricks B1 and B2 and three small glasses inserted in each of bricks C1 and C2 have the same sizes but different thickness as shown in Table 1. Figure 2 shows the locations and depth of glasses embedded in bricks B and C: the large glass located near the brick's surface and thee small glasses located deeper in the middle of brick. Bricks A1 and A2 contain only cement for use as the control samples.

Table 1. Dimensions of glass inserts used in Samples B and C.

Thickness	Size	Bricks
1/8 in.	8 in. × 4.5 in.	B1, B2
1/8 in.	1 in. × 2.5 in	C1, C2
1/16 in.	1 in. × 2.5 in.	C1, C2
3/16 in.	1 in. × 2.5 in.	C1, C2

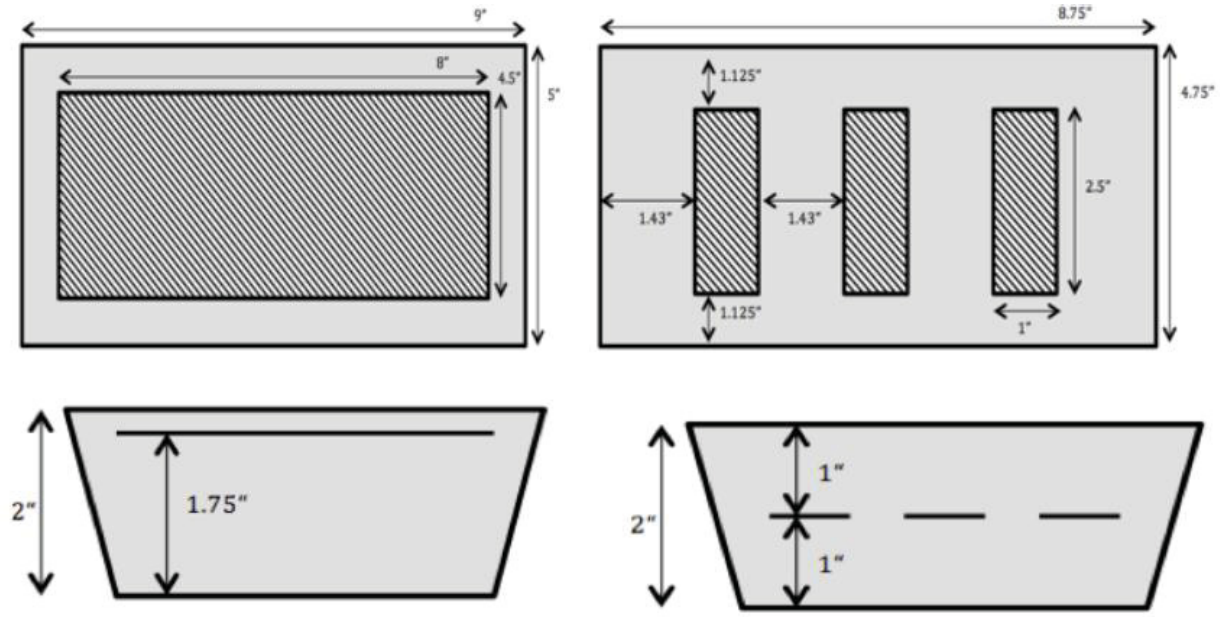

Figure 2. Bricks B (left) and C (right): dimensions and placement of glass inserts.

Curing Process

The bricks were removed from the molds 24 hours after casting and were cured for the next 24 hours in water at room temperature. After the initial curing, the two sets of samples were cured separately under different conditions. The first set that consisted of bricks A1, B1, and C1 was cured in water at room temperature and the second set that consisted of bricks A2, B2, and C2 was cured in normal NaOH solution at 80°C. The curing conditions for the second set were followed the ASTM C1293 (2008) standard for more ASR accelerated curing because exposure to NaOH increases the alkali content of the cement. The water-cured samples act as the baseline measurement for detection of ASR gel. Table 2 summarizes composition and curing conditions for the two sets of three brick samples.

Table 2. Summary of composition and curing conditions of the two set of small brick samples.

Set	Bricks	Aggregate	Curing Condition
1	A1	Cement only (baseline)	Water at room temperature
	B1	One large glass near the top	Water at room temperature
	C1	Three small glasses in the middle	Water at room temperature
2	A2	Cement only	NaOH solution at 80°C
	B2	One large glass near the top	NaOH solution at 80°C
	C2	Three small glasses in the middle	NaOH solution at 80°C

3.1.2 Medium-Sized Concrete Slab

While there can be much gained from studying these bricks, scaling up the size of the concrete samples will yield valuable information. With the ultimate objective being detected ASR in real-world structures, it is necessary that a medium-sized concrete slab be constructed that is closer to realistic structural sizes in NPPs.

This medium-sized slab was cast on December 21, 2015 and has dimensions of 2 ft × 2 ft × 6 in. Figure 3 shows an image of the slab immediately after the mold was removed.

Figure 3. 2 ft × 2 ft × 6 in. dimension concrete slab.

A medium-sized slab like this one presents challenges in material required for casting, space for curing, maneuverability for nondestructive testing, transporting from casting facility to curing and NDE facility, and diagnosis of damage.

3.1.2.1 Aggregates. Four types of aggregate are placed in pockets at a depth of 3 in. in quadrants of the slab (Figure 4). The aggregates are placed in pockets instead of being dispersed throughout the slab so that the reactivity of each aggregate can be determined independently. Additionally, since the locations of the pockets of aggregate are known, this information can be used to validate the localization of ASR from the nondestructive testing. The four types of aggregates used are as follows:

1. Pure silica – powder from local ceramic shop
2. Wells – coarse aggregate from Wells, Maine, donated by University of Alabama
3. Placitas – coarse aggregate from Placitas, New Mexico, donated by University of Alabama
4. Spratt – coarse aggregate from Spratt quarry in Ontario, Canada, donated by the Ontario Ministry of Transportation.

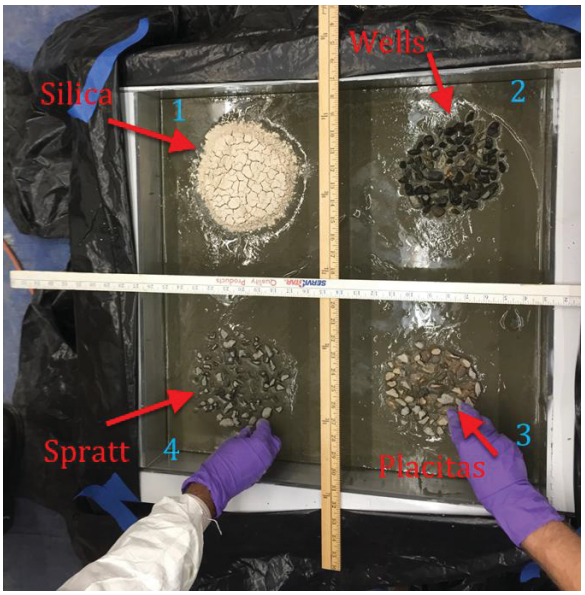

Figure 4. Labeled pockets of aggregate in the slab.

3.1.2.2 Curing Tub. A stainless-steel piece of sheet metal is bent and welded along the seams to form a watertight tub with four sides. This tub is used for curing the slab. In Figure 5, the slab is being lowered into the tub by a crane located at the Laboratory for Systems Integrity and Reliability. ASR is a slow process that can take several decades to come to fruition; in the laboratory there are several things that can be done to accelerate this process. Using sodium hydroxide, NaOH, in the mix water or placing the cured concrete in a NaOH solution causes an increase in PH. Selecting highly reactive siliceous aggregates or even glass will provide an available source of silica. Lastly, curing the specimens at temperatures around 60°C has been found to accelerate ASR. The slab was cured above water in 100% humidity and 60°C in a controlled environmental chamber.

Figure 5. Slab sitting on the frame and being lowered into the tub.

3.2 Damage from Alkali-Silica Reaction in Medium-Sized Concrete Slab

From December 21, 2015 to September 2016, the 2 ft × 2 ft × 6 in. dimension concrete slab showed no visual signs of degradation due to ASR. In October 2016, first visual evidence of degradation due to ASR was observed. Since then, the degradation related damage has become increasingly pronounced. The first indication of damage was detected by the two vibration-based NDE methods, NIRAS and VAM. Then hairline cracks were observed on the surface of the slab, and now an ASR gel effluent and whitish powder are seeping out of the slab. Interestingly, no significant deformation has been observed thus far – this may be due to placing the aggregates in pockets rather than dispersing them throughout the slab as would be seen in typical concrete.

In Figure 6, the red squares identify where the damage has been found on the sides of the slab and correspond to images of damage in Figure 7, Figure 8, and Figure 9 respectively.

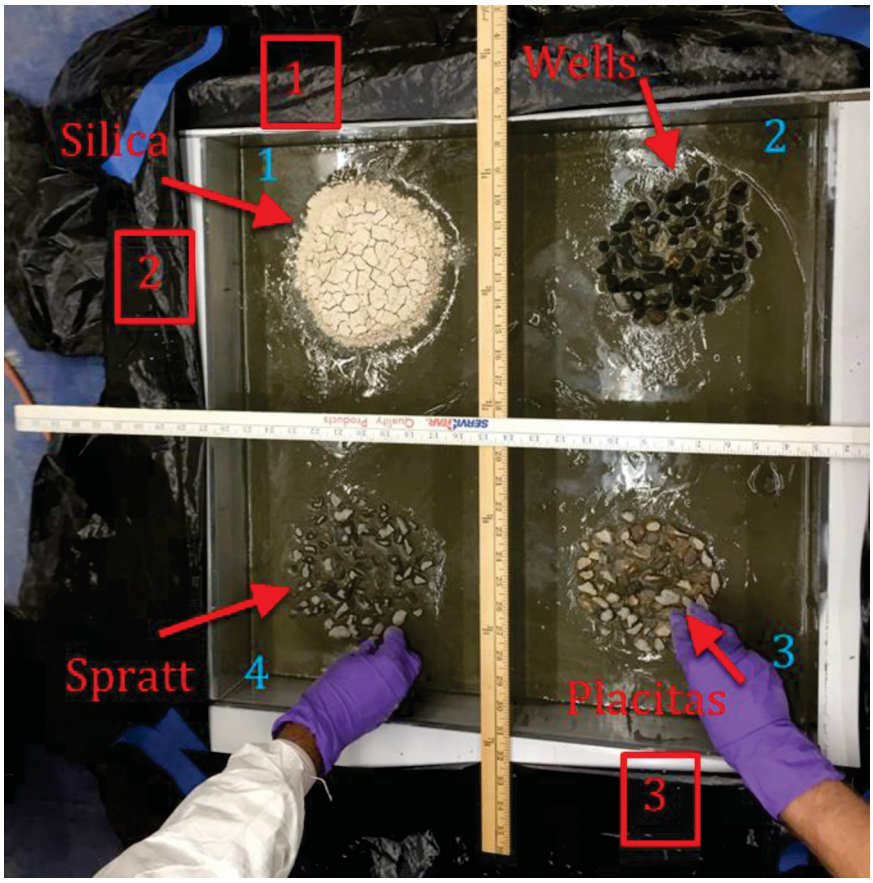

Figure 6. Pockets of aggregate in the slab during casting with red squares identifying visually observed cracks and effluence on the side of the slab.

Figure 7. Damage location 1 – cracking and powder effluence.

Figure 8. Damage location 2 – clear gel effluence.

Figure 9. Damage location 3 – cracking and powder effluence.

The whitish powder or gel effluents detected in Figure 7 to Figure 9 (the figure captions indicate whether powder or gel was observed) were scraped from the slab and collected so that Inductively Coupled Plasma-Optical Emission Spectroscopy (ICP-OES) could be conducted at the Vanderbilt University Civil & Environmental Engineering Laboratory to determine if the substance was ASR gel. Table 3 presents the results from ICP-OES with the breakdown of the elements in both the gel effluent and the whitish powder, confirming that the effluent material was the product of alkali-silica reaction. Note that the volume of gel collected was larger than whitish powder and hence the mg/L values are larger for the gel.

Table 3. ICP-OES results for the gel and powder samples.

	Gel	Powder
	mg/L	mg/L
Aluminum	1.3	0.1
Calcium	3.3	4.0
Potassium	520.0	2.9
Sodium	1,100.0	1.7
Sulfur	2.0	0.0
Silicon	1,600.0	2.0

4. NONDESTRUCTIVE EVALUATION TECHNIQUES

This research investigates the monitoring of degradation in concrete due to ASR via full-field and multi-physics techniques. Effective combinations of full-field and multi-physics techniques need to be identified for different types of concrete structures under different loading and operating conditions. In this study, the multi-physics approaches considered are visual, vibrational, and thermal. The monitoring techniques are studied on the medium concrete slab.

4.1 Measuring Mechanical Deformation

The telltale sign of a concrete structure experiencing ASR is expansion. For the medium-sized cement slab, expansion is measured mechanically using calipers. DIC is another technique to measure deformation and it is performed on the large concrete slab at the University of Tennessee, Knoxville as discussed in Section 4.5.

4.1.1 Mechanical Deformation Test Setup

Calipers are used to take length measurements, and comparison of these measurements overtime reveals whether any deformation has occurred. The calipers shown in Figure 10 and Figure 11 have a maximum length of 1 ft and a resolution of .001 in. Steel nails were cast into the concrete samples in order to provide a reference points for length measurements.

Figure 10. Calipers used for mechanical deformation measurements.

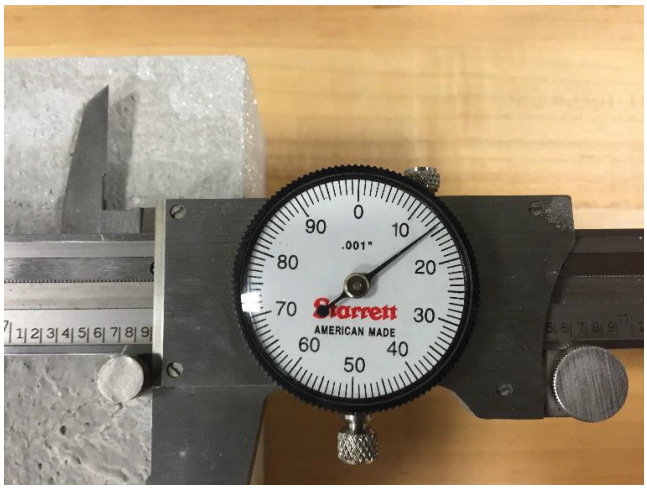

Figure 11. Calipers being used to measure the distance between nails.

4.1.2 Mechanical Deformation Results

There has been no noticeable expansion of the medium-sized slab since it was cast in December 2015. This is due to placing the reactive aggregates in a single layer in four pockets rather than using them throughout the slab; thus the volume of aggregate is very small compared to the size of the slab. This causes the ASR reaction to be localized around the pockets of aggregates, thus any expansion contributed by ASR is negligible compared to the volume of the slab. In other words, deformation is a global measure of the overall expansion of the structure due to ASR; thus deformation measurement is unable to detect the presence of ASR in the medium-sized slab. However, the vibration-based NDE methods are able to detect ASR in this slab, as discussed in following Section 4.2 and Section 4.3.

4.2 Nonlinear Impact Resonance-Acoustic Spectroscopy

NIRAS is a vibration-based NDE method that detects nonlinearities, (i.e., damage), via shifts in resonant frequencies. A larger shift indicates more severe damage.

4.2.1 NIRAS Test Setup

Impact from a modal hammer is used to excite the samples over a broadband frequency range. The sample is impacted on the top surface at the same location for each hit (blue crosses in Figure 12). The selection of impact location is selected by avoiding major lines of symmetry, which improves the response. Two accelerometers are used to measure the samples vibrational response (as shown in Figure 13). The accelerometers are also placed on the top surface of the slab. The slab is placed on a foam mat, which represents a free-free condition and allows for reduced noise in the data. Both impact force from the hammer and vibrational response from the accelerometers are collected using a data acquisition system. The collected data are processed in MATLAB.

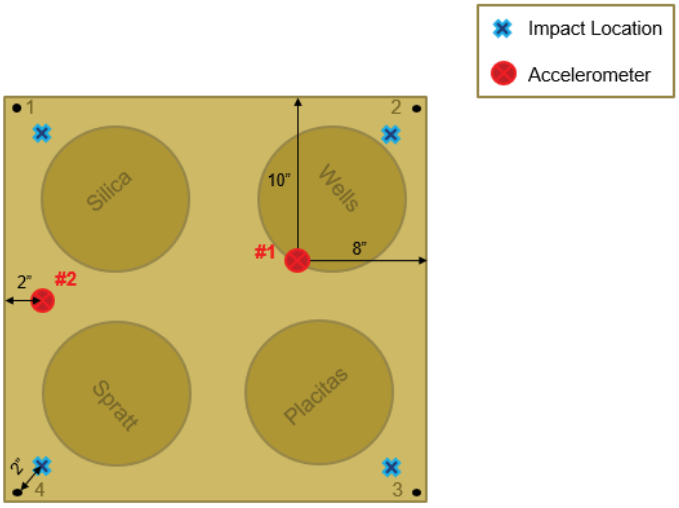

Figure 12. A schematic representation showing placement of accelerometers and impact locations.

4.2.2 NIRAS Results

Using the setup shown in Figure 12, the impact from the hammer was applied at five different impact force amplitudes at each of the four impact locations. The test was repeated five times for each force amplitude and for a given impact location. The impact location numberings correspond to the corners the impacts are closest. Figure 14 and Figure 15 plot the power spectral density (PSD) of the vibrational response across a frequency range from 0 to 5 kHz for accelerometer 1 and 2, respectively. Each of the five colored-coded curves represent different impact force amplitudes. In general, the amplitude of the PSD curve increases as the force amplitude increases because there is more energy input into the slab. Notice that the plots vary across the four impact locations and between the two accelerometers. This is expected because different locations are more sensitive to one mode shape than another and therefore the amount of vibrational energy recorded at a particular frequency will vary over location.

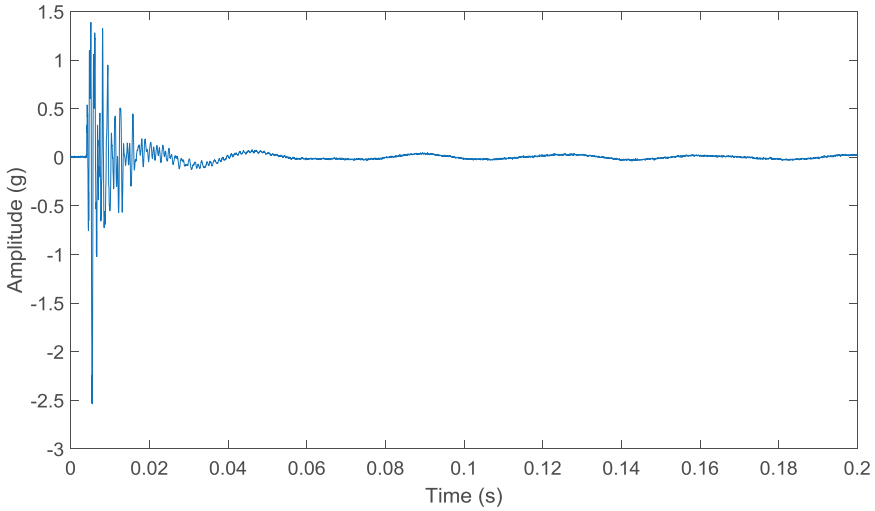

Figure 13. Vibration response of a concrete slab measured by an accelerometer after modal hammer impact.

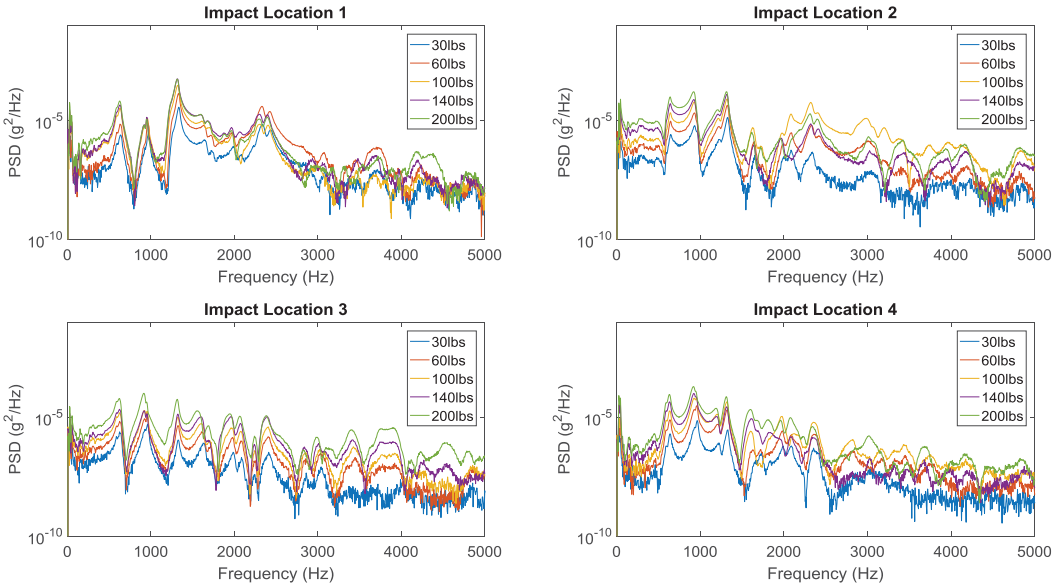

Figure 14. Power spectral distribution generated using the data collected by the accelerometer 1 data at different impact locations.

From the raw PSD plots, it is difficult to say whether a shift in the resonant frequency occurred with increased impact force. In Figure 16 and Figure 17 the plots are zoomed in to the peaks (i.e., resonant frequencies), of the PSD plots. For additional ease, drawn on the figures are a solid vertical line that originates from the peak on the 30lb curve (i.e., blue) and a dashed line that goes from the peak on the 30lb curve through the peak on the 200lb curve.

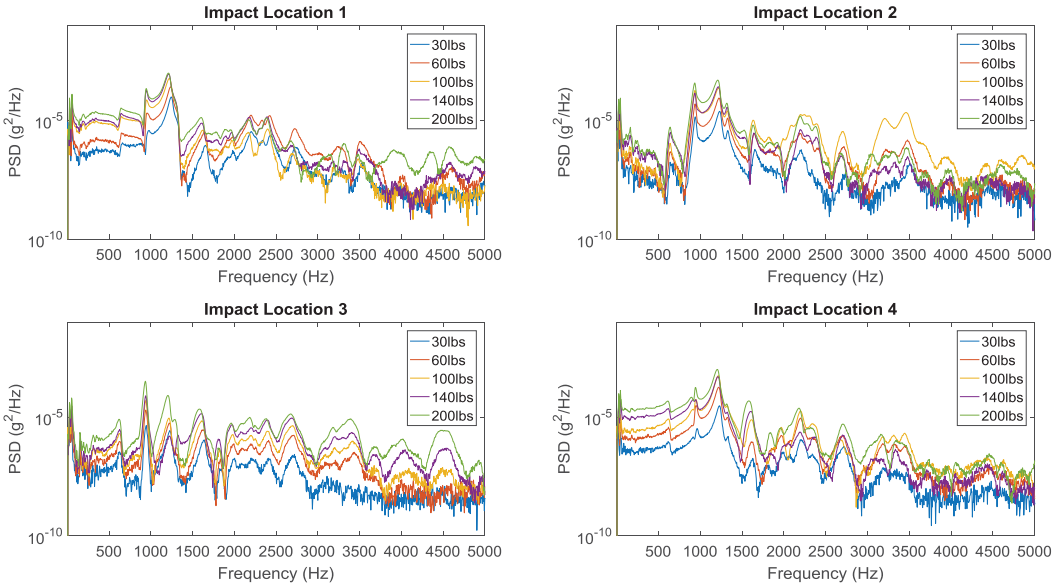

Figure 15. Power spectral distribution generated using the data collected by the accelerometer 2 data at different impact locations.

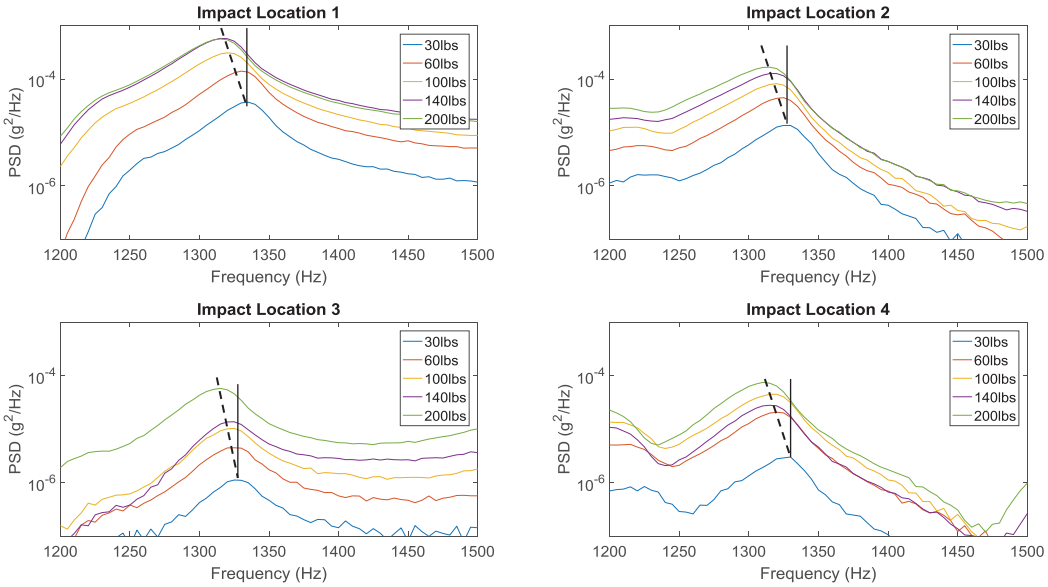

Figure 16. Accelerometer 1 frequency shift at resonant frequencies (December 2016).

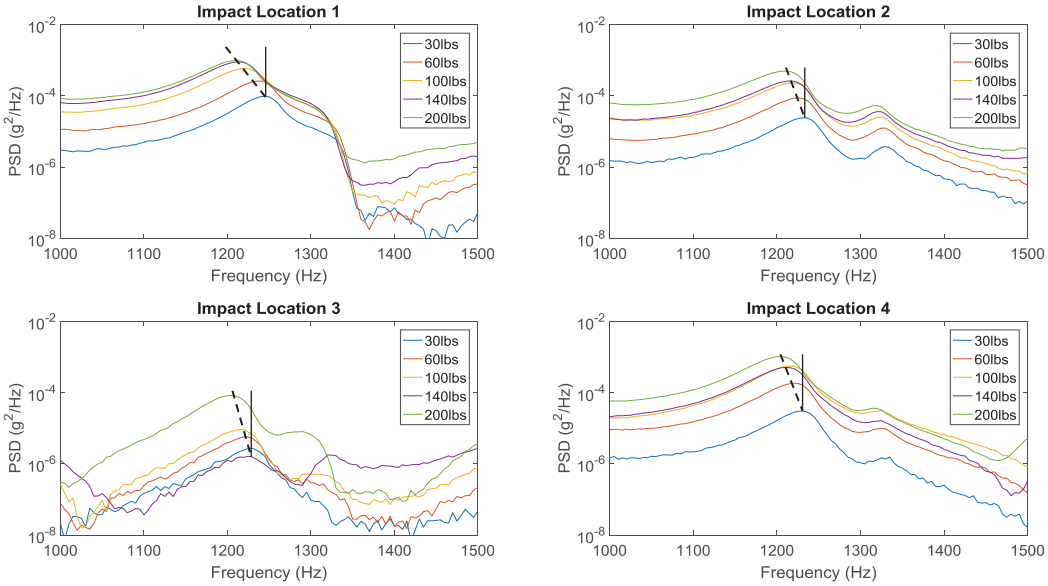

Figure 17. Accelerometer 2 frequency shift at resonant frequencies (December 2016).

The frequency response in December 2016 is compared to the frequency response of the data collected earlier in January 2016. A clear frequency shift is observed in Figure 16 and Figure 17 compared to the frequency response in Figure 18 for Accelerometer 1. Recall that concrete gains strength over time, and resonant frequency is dependent on stiffness. The data in Figure 18 is from January 2016, when the concrete had 28 days to cure, which is the standard full curing period. This is why the resonant frequency captured by accelerometer 1 for the 3rd mode is ~1140 Hz instead of ~1330 Hz. During the experiment in January 2016, data was collected for shorter time duration; hence the resolution (i.e., number of data points along the frequency axis) of Figure 18 is lower than that for the data collected in December 2016.

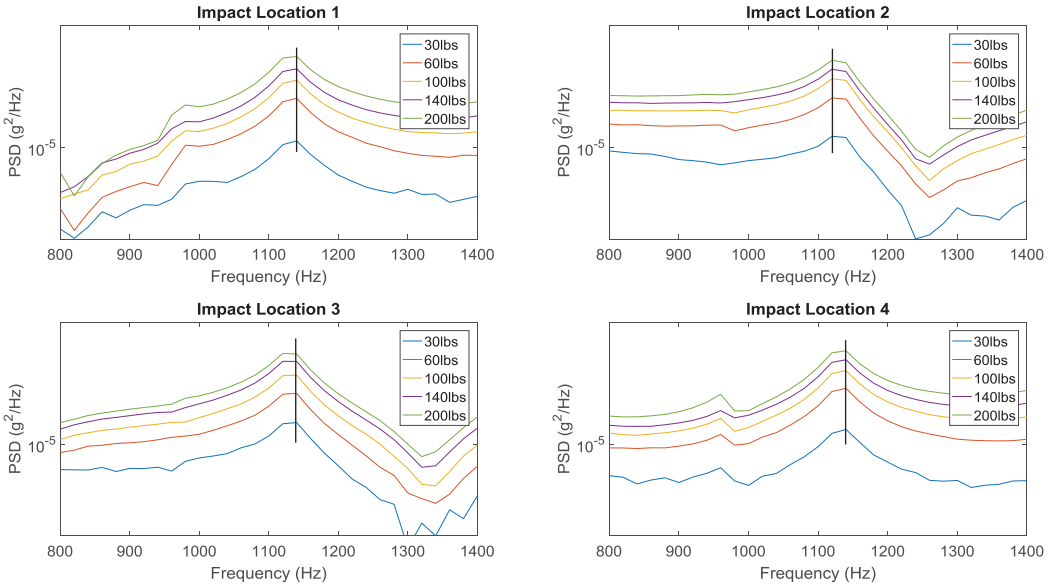

Figure 18. Accelerometer 1 zoomed into frequency shift at resonant frequency (January 2016).

In addition, it was observed that some natural frequencies exhibit a greater shift, while other natural frequencies exhibit little to no shift. This is an interesting observation that only some natural frequencies display a strong shift. Based on this observation, it is concluded that only corresponding mode shapes are sensitive to the damage. By mapping the particular mode shape that is sensitive to damage, it might be possible to infer the location of the damage. Using mode shapes to localize damage is a potential area of future work. Overall, the results in both Figure 16 and Figure 17 show frequency shifts, thus detecting and confirming the presence of damage.

4.3 Vibro-Acoustic Modulation

VAM is another vibration-based NDE method, but it detects nonlinearities by mixing a high and a low vibration wave. Nonlinearity will produce 'sidebands' in the frequency domain while a linear structure will follow the law of superposition.

4.3.1 VAM Test Setup

Two piezo-stack actuators are used. One is dedicated to excite the slab with "pump" frequency and another is dedicated to excite the slab with "probe" frequency. Originally a modal impact hammer was used to create an impulsive load used for the low frequency pump, but the results for these experiments were very noisy. Therefore, an instrumented actuator was used subsequently. The pump and probe were placed at different locations along the slab with varying probing frequencies and the results were recorded.

4.3.1.1 Pumping Frequency. The fundamental frequency of the slab was found both computationally and experimentally. When the hammer was used to excite the slab, there were multiple peaks found at the lower frequencies, the first and more prominent being 920 Hz. Using a basic finite element model of a plan concrete structure the same size as this slab, the computational frequency was found to be 936 Hz. The difference in these frequencies is likely due to the deformation and voids in the actual slab material that were not considered in the model. The frequency of 920 Hz was pumped through the sample using a piezo-stack actuator to minimize the noise caused by the hammer. Figure 19 and Figure 20 show the comparison of PSD plots observed from the basic impact hammer and the piezo-stack

actuator. The figures also show that the latter has very little noise compared to the former. Therefore, the instrumented actuator was used in further study. The location for the pumping actuator was kept constant in most experiments.

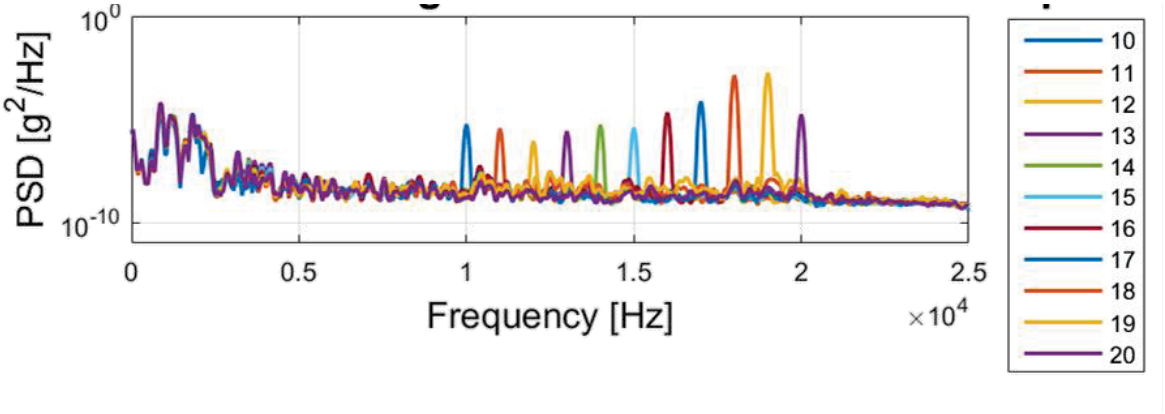

Figure 19. PSD plots corresponding to excitation by an impact hammer. Each color curve is a different probing frequency in kHz.

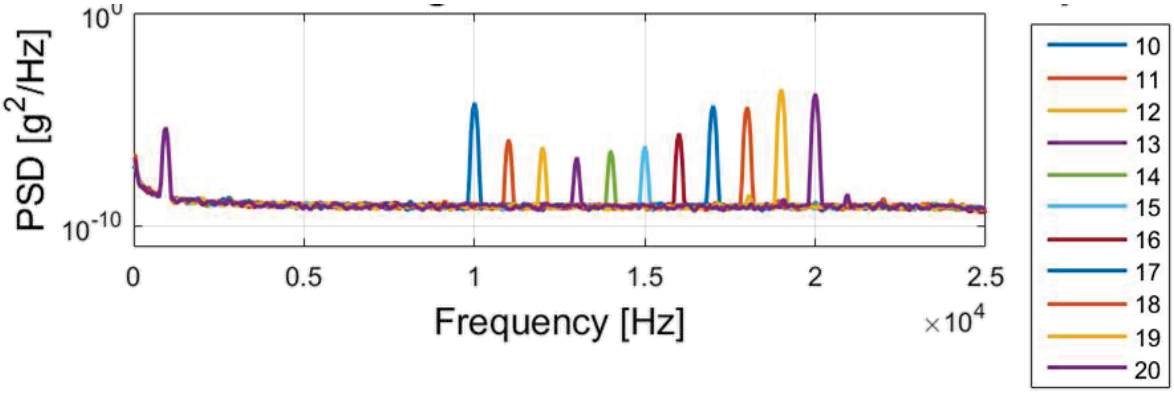

Figure 20. PSD plots corresponding to excitation at 920-Hz by an actuator. Each color curve is a different probing frequency in kHz.

4.3.1.2 Probing Frequency. Probing frequencies ranging from 10 to 20 kHz were used on the slab. The amplitude and location of the probing frequency was also varied in different experiments. In general, a higher probing to pumping frequency ratio is preferred in the testing; however, the maximum probing frequency was limited by the data acquisition system used for collecting the accelerometer data.

4.3.1.3 Accelerometers. A maximum of eight accelerometers are placed on the concrete slab and connected to the data acquisition system. The locations of these accelerometers are varied for each experiment. The accelerometers were calibrated biweekly to ensure accuracy.

4.3.2 VAM Results

Using a basic setup for the experiment shown below, sidebands were found in the PSD plots of the medium concrete slab. Similar to NIRAS, VAM testing was able to detect damage. Experimental testing was conducted further to try and localize the damage in the structure and upon investigation, it was noted that during testing only some accelerometers showed the presence of sidebands while others did not. This

meant that for one given pump and probe configuration some portions of the slab would detect the damage while others would not.

The next experimental variable investigated was the probing frequency. As the probing frequency was changed, the presence of sidebands varied. The same accelerometer location that showed sidebands for one probing frequency did not always show sidebands for another frequency. As noted in Section 2.2.5, a higher probing to pumping frequency ratio is preferred in VAM testing. Thus a 20-kHz probing frequency could be assumed to produce the best results for testing; however, this is still uncertain. Since 20-kHz was the maximum probing frequency that could be used in these trials, the amplitude of the probing frequency was decreased to improve the results for damage localization.

Accelerometer locations, probing frequency, and amplitudes are the variables that have significant impact on the results. Both pump and probe locations are varied for the following experimental configurations. Figure 21 shows different configurations of probing and pumping actuators. Figure 22–Figure 37 and Table 4–Table 9 show the experimental configuration and the results obtained for each experimental configuration. The results identify the accelerometers for each set up that showed sidebands in the results. If the location showed sidebands in the PSD plot, it is denoted as "1" and if no sidebands are observed, it is denoted as "0". The accelerometers were calibrated biweekly to ensure accuracy. In some measurements, one of the accelerometers will fail to capture the signal; such cases are indicated as missing data and denoted as " - ".

In this section, the pumping and probing actuator locations for various experiments are indicated by the scheme shown in Figure 21. The Q values represent the quadrants corresponding with the corner numbers as seen in Figure 6. Q1 is in the quadrant near Corner 1 and Q1_3 represents the third sub-quadrant (sub-quarter closest to Corner 3) within the first quadrant near Corner 1. Within the quadrant locations, the probe or pump was placed in the center. Seven different accelerometer configurations were used in testing, and the results for each configuration are discussed below.

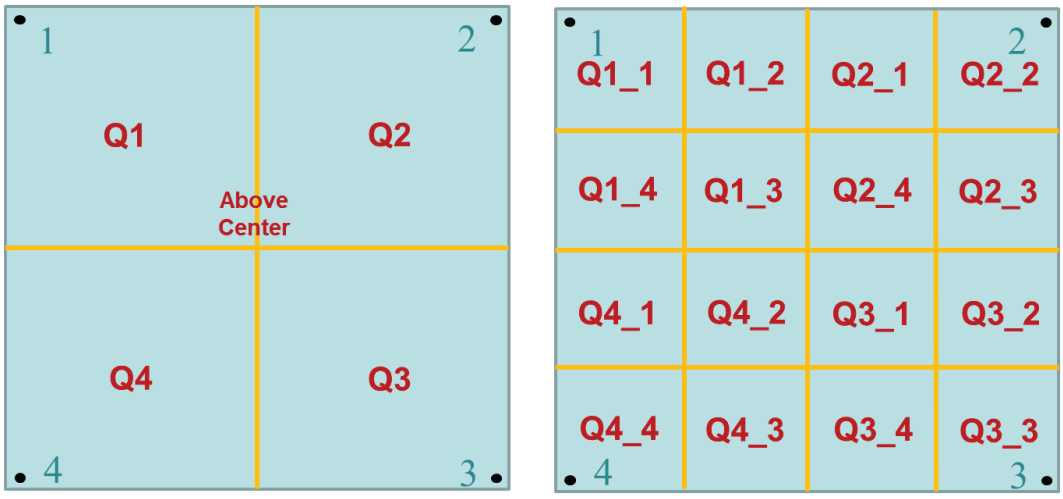

Figure 21. Testing locations for pumping actuators and probing actuators.

4.3.2.1 Configuration 1

In this configuration, eight accelerometer sensors are used and their locations (red crosses) are shown in Figure 22. The pumping actuator is located 1 in. above the centerline shown in Figure 21. The probing actuator location, probing frequency, and probing excitation amplitude are varied (marked as blue cross in Figure 22). Figure 22 and Figure 23 show the schematic and actual placement of actuators and sensors respectively. Figure 24 shows a sample PSD plots generated using the data collected from accelerometers 3 and 6 for 20-kHz probing frequency (amplitude = 500 mV amp) in Q4 and 920-Hz pumping frequency. Observe in Figure 24, accelerometer 6 shows sidebands but no sidebands are observed at accelerometer 3.

Figure 25 shows the presence or absence of sidebands at different sensor locations for the same probing excitation. Then Table 4 shows the results (i.e., presence or absence of sidebands) for all the probe locations, frequencies, and amplitudes. For this configuration, it is observed that sidebands were observed at some accelerometer locations and not at remaining locations. Table 4 summarizes the outcomes when the slab is excited with two probe amplitudes and probe frequency ranging for 18-kHz to 20-kHz. For the combination that the probe was placed in Q4, excited with 20-kHz and amplitude of 100 mV amps, only one accelerometer showed sidebands. Alternatively, for the excitation amplitude of 500 mV amps, 5 sidebands are observed. This highlights the fact excitation amplitude has an impact of presence or absence of sidebands at different accelerometer locations.

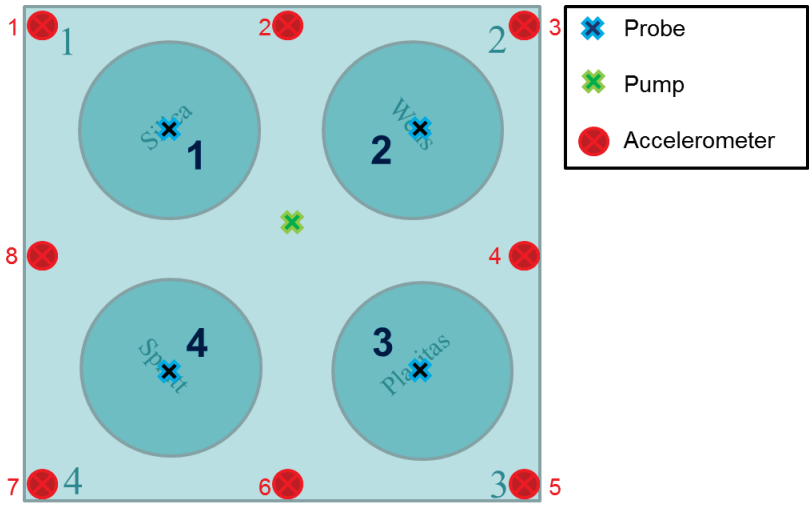

Figure 22. Schematic setup for accelerometers placed around the slab's perimeter.

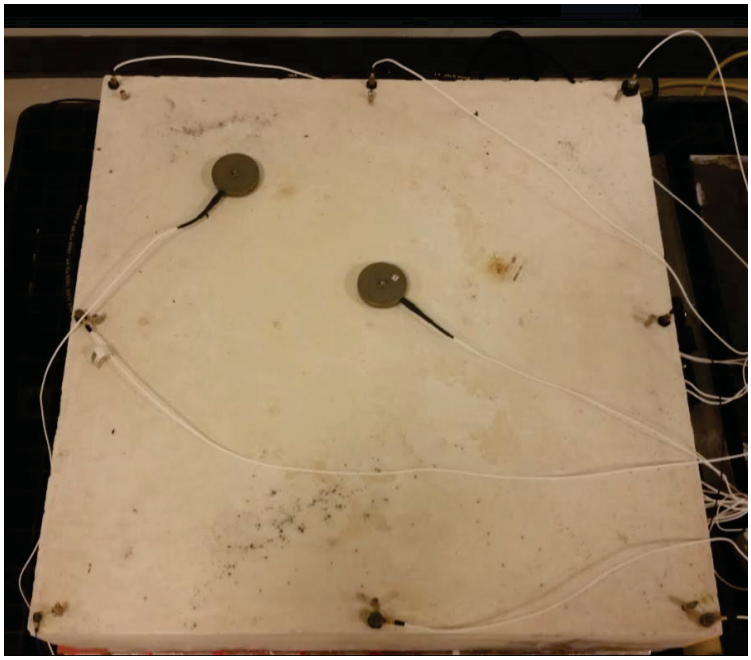

Figure 23. Experimental setup for accelerometers placed around the slab's perimeter.

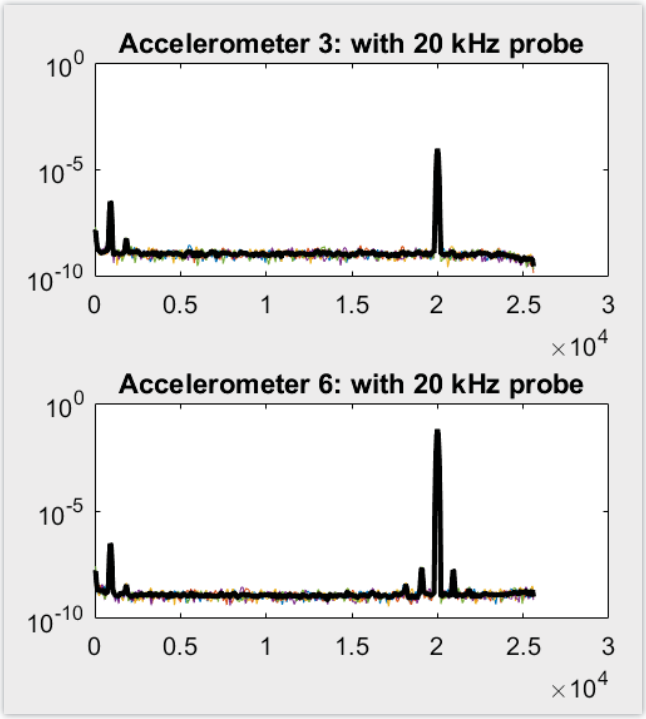

Figure 24. PSD plots used for sideband detection for 20-kHz probing frequency (amplitude = 500 mV amp) in Q4 and 920-Hz pumping frequency. Sidebands are observed at accelerometer 6 and no sidebands are observed at accelerometer 3.

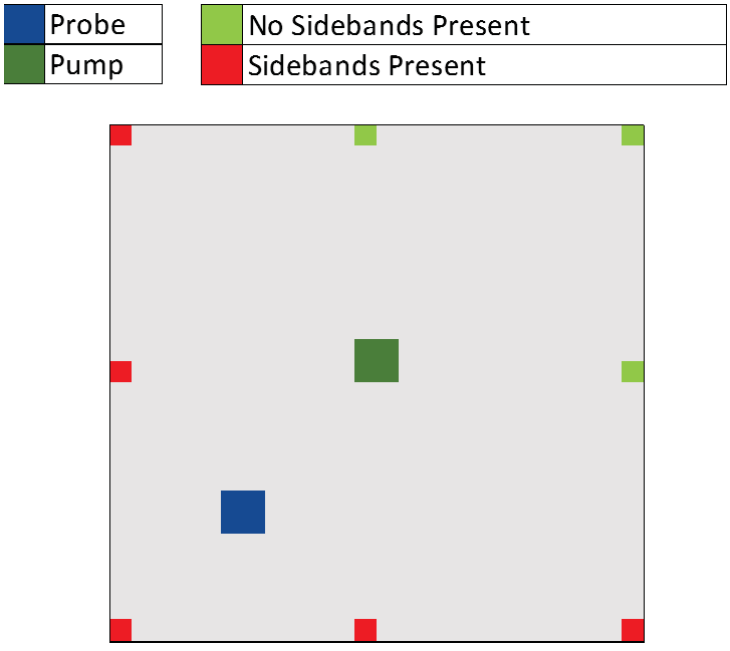

Figure 25. Sideband detection for 20-kHz probing and 920-Hz pumping frequencies.

Table 4. VAM results for Figure 22 and Figure 23(1: sidebands; 0: no sidebands; - : missing data).

Pump Location	Probe Location	Probe Amplitude (mV amps)	Probe Frequency (kHz)	Observation Points (Accelerometer)							
				1	2	3	4	5	6	7	8
Above Center	Q1	500	18	0	0	0	0	0	0	0	0
			19	0	0	0	0	0	1	1	0
			20	0	0	0	0	0	1	1	0
		100	18	0	0	0	0	0	0	0	0
			19	0	0	0	0	0	0	0	0
			20	0	0	0	0	0	0	0	0
	Q2	500	18	0	-	-	0	0	0	0	0
			19	0	0	0	0	0	0	0	0
			20	0	0	0	0	0	0	0	0
		100	18	0	0	0	0	0	0	0	0
			19	0	0	0	0	0	0	0	0
			20	0	0	0	0	0	0	0	0
	Q3	500	18	0	0	0	0	0	0	0	0
			19	1	0	0	1	1	1	1	1
			20	0	0	0	0	1	1	1	1
		100	18	0	0	0	0	0	0	0	0
			19	0	0	0	0	1	0	0	0
			20	0	0	0	0	0	0	0	0
	Q4	500	18	1	0	0	1	1	1	1	1
			19	1	0	0	1	1	1	1	1
			20	1	0	0	0	1	1	1	1
		100	18	0	0	0	0	0	0	0	1
			19	0	0	0	0	0	0	0	0
			20	0	0	0	0	0	0	0	1

4.3.2.2 Configuration 2

In this configuration, eight accelerometer sensors are used and their locations (red crosses) are shown in Figure 26. The pumping actuator is located 1 inch above the centerline. Probing actuator location, probing frequency, and probing excitation amplitude are varied. Figure 26 and Figure 27 show the schematic and experimental setup for this configuration respectively. Table 5 shows the results (i.e., presence or absence of sidebands) for all the probe locations, frequencies and amplitudes. The setup shown in Figure 26 and Figure 27 showed no evidence of sidebands for different combination of probe location, probing frequency and amplitude. This highlights the fact that placement of sensors and actuators impact the experimental outcomes.

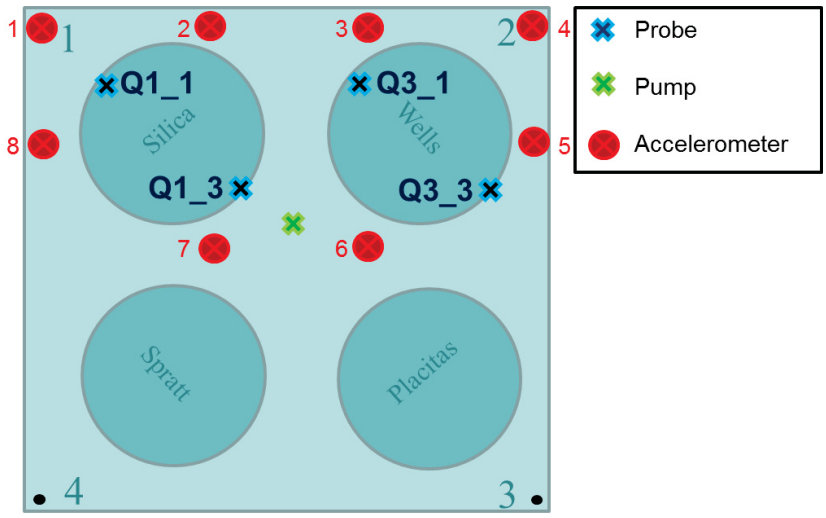

Figure 26. Schematic setup for accelerometers on the slab.

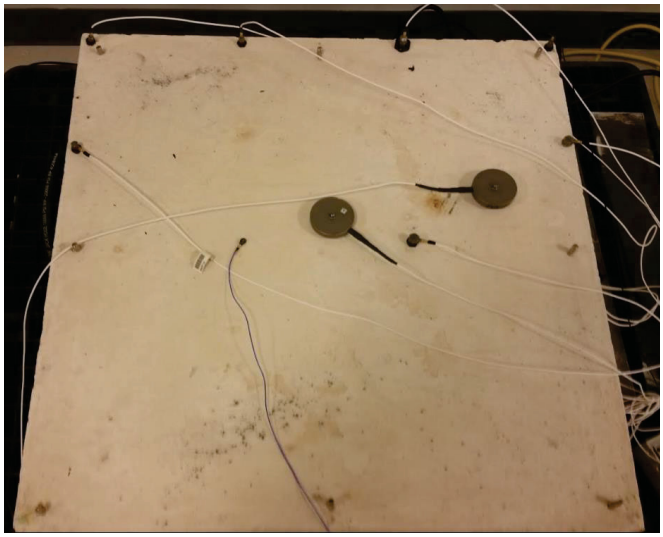

Figure 27. Experimental setup for accelerometers on the slab.

Table 5. VAM results for Figure 26 and Figure 27 (1: sidebands; 0: no sidebands; - : missing data).

Pump Location	Probe Location	Probe Amplitude (mV amps)	Probe Frequency (kHz)	Observation Points							
				1	2	3	4	5	6	7	8
Above Center	Q1_1	100	19	0	0	0	0	0	0	-	0
			20	0	0	0	0	0	0	-	0
	Q1_3	100	19	0	0	0	0	0	0	-	0
			20	0	0	0	0	0	0	-	0
	Q2_1	100	19	0	0	0	0	0	0	0	0
			20	0	0	0	0	0	0	0	0
	Q2_3	100	19	0	0	0	0	0	0	-	0
			20	0	0	0	0	0	0	-	0

4.3.2.3 Configuration 3

In this configuration, eight accelerometer sensors are used and their locations (red crosses) are shown in Figure 28. The pumping actuator is located 1 inch above the centerline. The probing actuator location, probing frequency, and probing excitation amplitude are varied. Figure 28 shows the schematic placement of the actuators and sensors. Then Table 6 summarizes the results (i.e., presence or absence of sidebands) for different combinations of probe locations, frequencies, and amplitudes. For this configuration, no sidebands were detected for different combinations of probe locations, frequencies and amplitudes. This highlights the fact that placement of sensors and actuators impact the experimental outcomes.

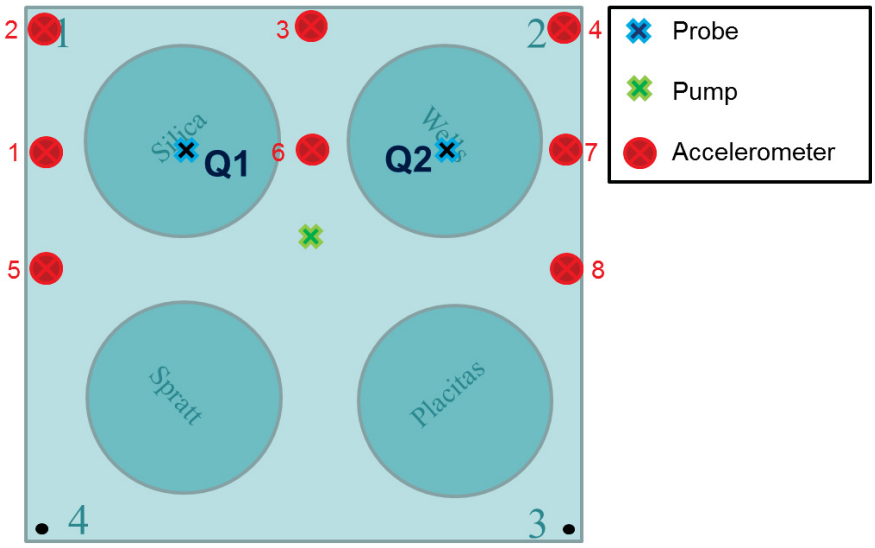

Figure 28. Schematic setup for accelerometers on the slab.

Table 6. VAM results for Figure 28 (1: sidebands present; 0: no sidebands; - : missing data).

Pump Location	Probe Location	Probe Amplitude (mV amps)	Probe Frequency (kHz)	Observation Points							
				1	2	3	4	5	6	7	8
Above Center	Q1	500	20	0	0	0	0	0	0	-	0
		400		0	0	0	0	0	0	-	0
		300		0	0	0	0	0	0	-	0
		200		0	0	0	0	0	0	-	0
		100		0	0	0	0	0	0	-	0
		50		0	0	0	0	0	0	-	0
	Q2	50	20	0	0	0	0	0	0	-	0

4.3.2.4 Configuration 4

In this configuration, eight accelerometer sensors are used and their locations (red crosses) are shown in Figure 29. The pumping actuator is located 1 inch above the centerline. The probing actuator location, probing frequency, and probing excitation amplitude are varied. Figure 29 and Figure 30 shows the schematic and experimental placement of the actuators and sensors respectively. Figure 31 shows a sample PSD plot for accelerometers 1 through 8, for 20-kHz probing frequency (amplitude = 200 mV amp) in Q3 and 920-Hz pumping frequency. Then Table 7 summarizes the results (i.e., presence or absence of sidebands) for all the probe locations, frequencies, and amplitudes. For the setup shown in

Figure 29 and Figure 30, some locations of the accelerometer displayed sidebands while no sidebands were observed at others accelerometer locations. As seen in Figure 31 only one accelerometer location for the probe on Q3 with a 200 mV amp and 20-kHz frequency showed the presence of sidebands. The location of this accelerometer is located at the midpoint between Corners 2 and 3.

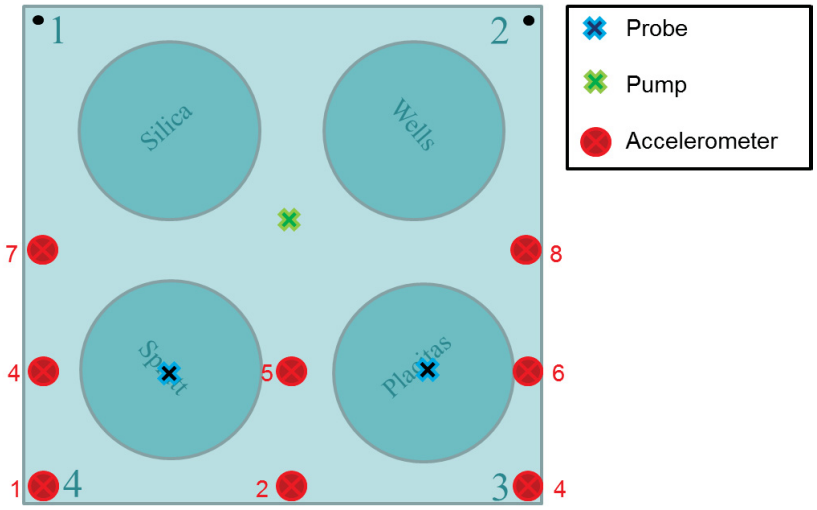

Figure 29. Schematic setup for accelerometers on the slab.

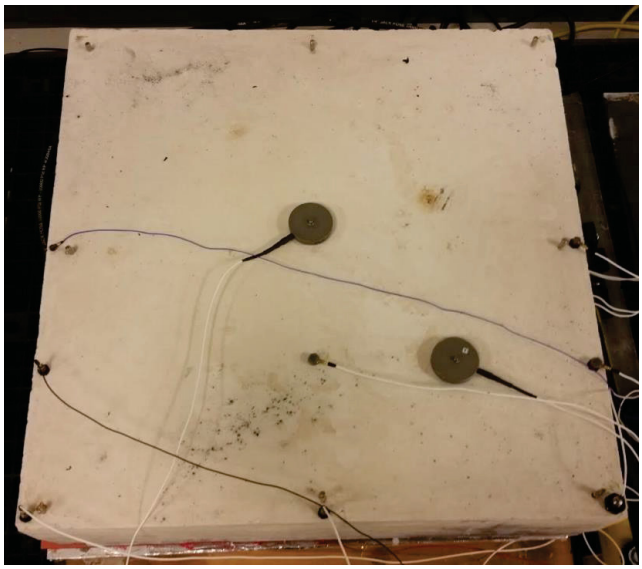

Figure 30. Experimental setup for accelerometers on the slab.

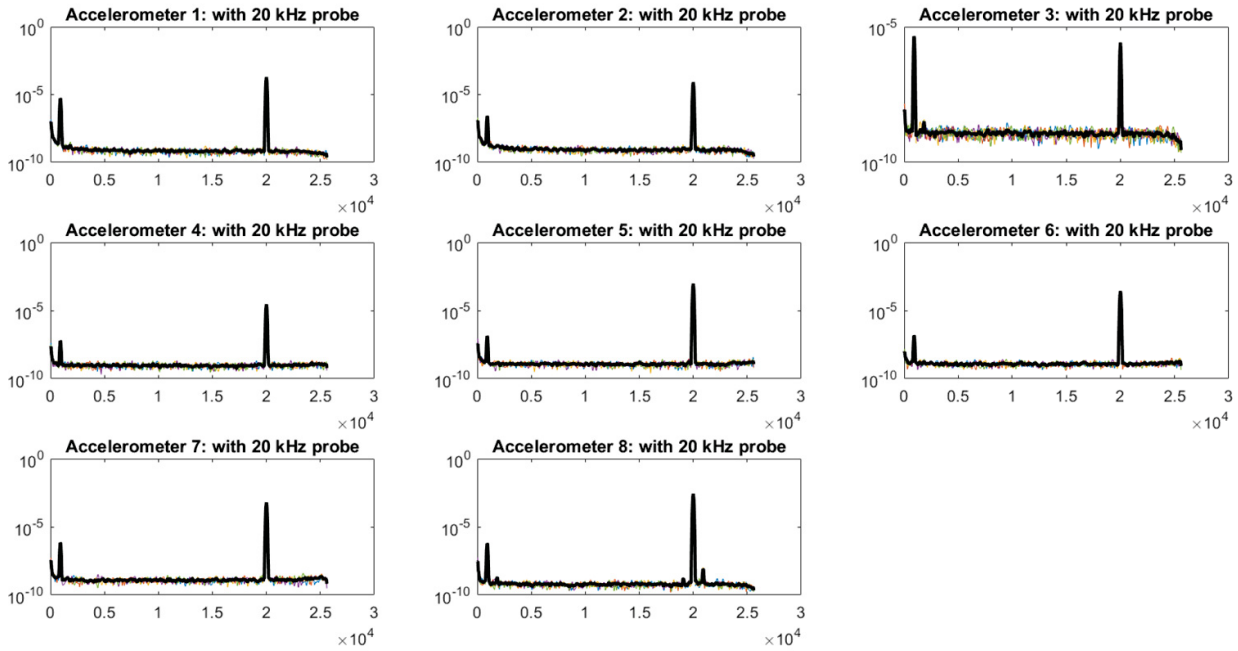

Figure 31. PSD plots used in sideband detection for the probe on Q3 with a 200 mV amp and 20-kHz probe.

Table 7. VAM results for Figure 29 and Figure 30. (1: sidebands; 0: no sidebands).

Pump Location	Probe Location	Probe Amplitude (mV amps)	Probe Frequency (kHz)	Observation Points							
				1	2	3	4	5	6	7	8
Above Center	Q3	500	20	0	1	0	0	1	0	0	0
		400		0	0	0	0	1	0	0	1
		300		0	0	0	0	0	0	0	1
		200		0	0	0	0	0	0	0	1
		100		0	0	0	0	0	0	0	0
		50		0	0	0	0	0	0	0	0
	Q4	500	20	0	0	0	0	0	0	0	0
		400		0	0	0	0	0	0	0	0
		300		0	0	0	0	0	0	0	0
		200		0	0	0	0	0	0	0	0
		100		0	0	0	0	0	0	0	0
		50		0	0	0	0	0	0	0	0

4.3.2.5 Configuration 5

In this configuration, eight accelerometer sensors are used and their locations (red crosses) are shown in Figure 32. The pumping actuator is located 1 inch above the centerline. The probing actuator location, probing frequency, and probing excitation amplitude are varied. Figure 32 shows the schematic locations of the actuators and sensors. Figure 33 shows a sample PSD plot for accelerometers 5 and 6, for 20-kHz probing frequency (amplitude = 100 mV amp) in Q3_1 and 920-Hz pumping frequency. Accelerometer 5 shows sidebands but accelerometer 6 shows no sidebands. Then Table 8 summarizes the results (i.e.,

presence or absence of sidebands) for all the probe locations, frequencies, and amplitudes. For the setup shown in Figure 32, some locations of the accelerometer displayed sidebands while no sidebands were observed at other accelerometer locations. As seen in Figure 33, only one accelerometer location for the probe on Q3_1 with a 100 mV amp and 20-kHz frequency showed the presence of sidebands. The location of this accelerometer is located 6 inches above Corner 4.

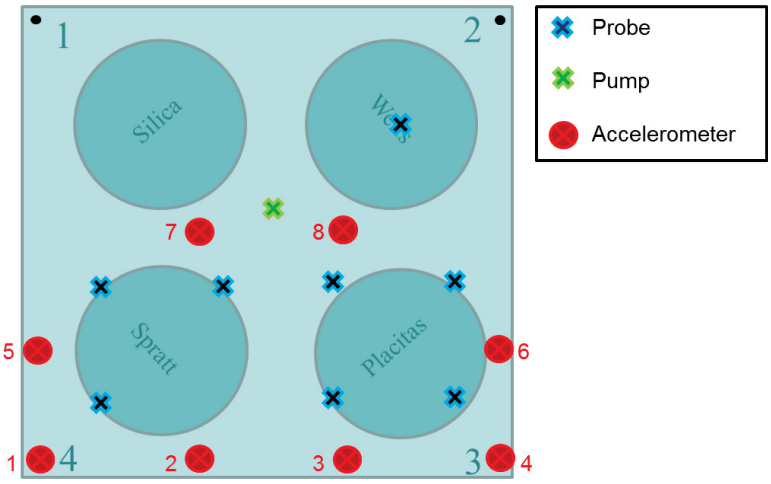

Figure 32. Schematic setup for accelerometers on the slab.

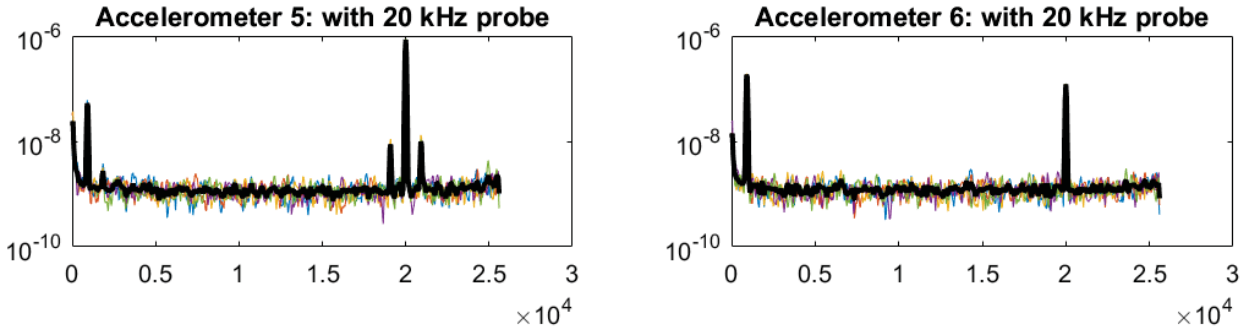

Figure 33. PSD plots used in sideband detection for the probe on Q3_1 with a 100 mV amp and 20kHz probe.

4.3.2.6 Configuration 6

In this configuration, eight accelerometer sensors are used and their 20 locations (red crosses) are shown in Figure 34. The pumping and probing actuator locations, probing frequency, and probing excitation amplitude are varied. Figure 35 shows the basic locations of four actuators and sensors. Figure 36 shows a sample PSD plot for accelerometers 1, 2, 3 and 4, for 17-kHz probing frequency (amplitude = 500 mV amp) in Q1, 920-Hz pumping frequency and accelerometer locations denoted in Figure 35. Figure 37 schematically shows the presence or absence of sidebands at different sensor locations for 18-kHz probing excitation (amplitude = 500 mV amp) for sensor and actuator locations denoted in Figure 34. Then Table 9 summarizes the results (i.e., presence or absence of sidebands) for all the pump and probe locations, frequencies and amplitudes. In the setup shown in Figure 34, some locations of the accelerometer displayed side bands while others did not. As seen in Figure 35, four accelerometer locations for the probe on Q1 with a 500 mV amp and 17-kHz frequency and the pump above the center showed the presence of sidebands. Most of these accelerometers were located along the sides of the slab near Corners 3 and 4. In Figure 37, 18-kHz probe and a 920-Hz pump actuator were used to conduct VAM testing. Figure 35 and Figure 36 show one group of four accelerometers used in the testing.

Accelerometers 1 and 4 show the presence of sidebands, while accelerometers 2 and 3 shows no sidebands.

Table 8. VAM results for Figure 32 (1: sidebands; 0: no sidebands; - : missing data).

Pump Location	Probe Location	Probe Amplitude (mV amps)	Probe Frequency (kHz)	Observation Points							
				1	2	3	4	5	6	7	8
Above Center	Q3_1	100	19	0	0	0	0	1	0	0	0
			20	0	0	0	0	1	0	0	0
	Q3_2	50	20	0	0	0	0	1	0	0	0
	Q3_3	100	19	0	0	0	0	0	0	0	0
			20	0	0	0	0	1	0	0	0
		50	20	0	0	0	0	0	0	0	0
	Q3_4	50	20	0	0	0	0	0	0	0	0
	Q4_1	50	20	0	0	0	0	0	0	0	0
	Q4_2	100	19	0	0	0	0	0	0	-	0
			20	0	0	0	0	0	0	-	0
	Q4_4	100	19	0	0	0	0	0	0	-	0
			20	0	0	0	0	0	0	-	0
	Q2	50	20	0	0	0	0	0	0	0	0

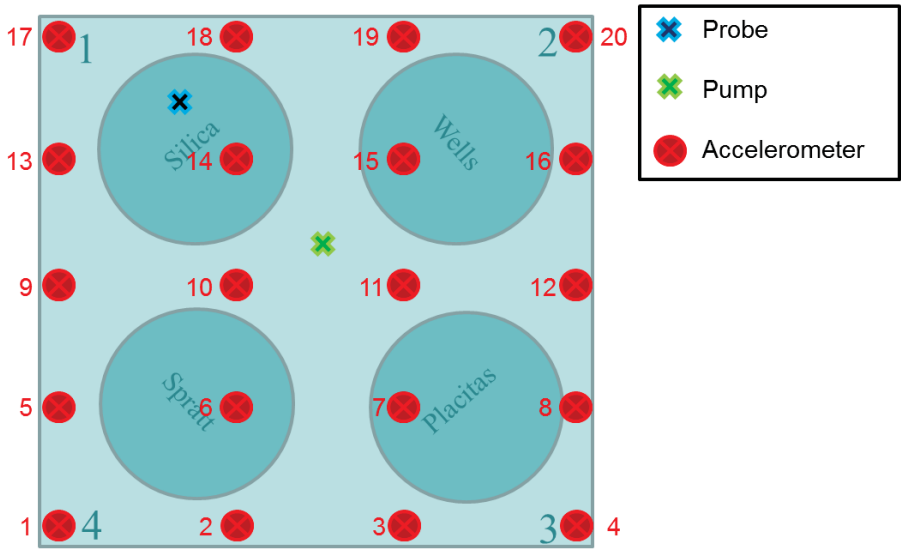

Figure 34. Schematic setup for accelerometers placed across the slab.

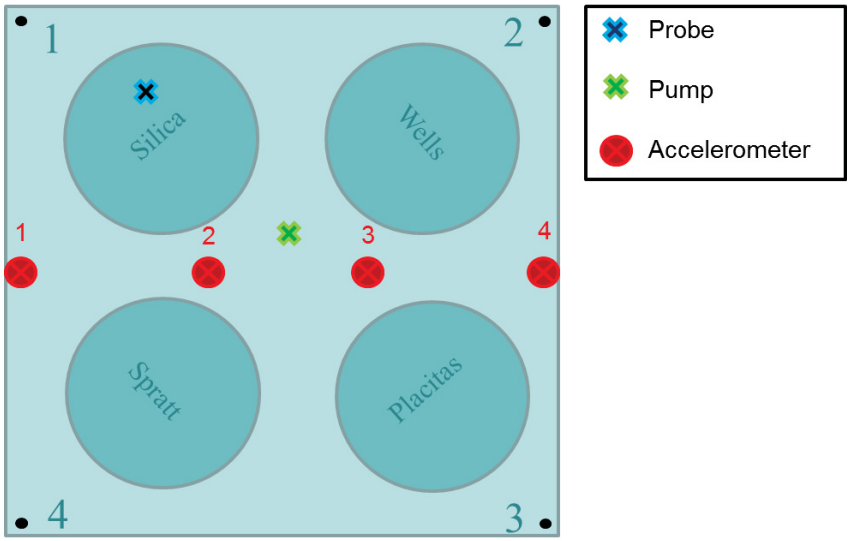

Figure 35. Schematic for the basic set up for VAM testing.

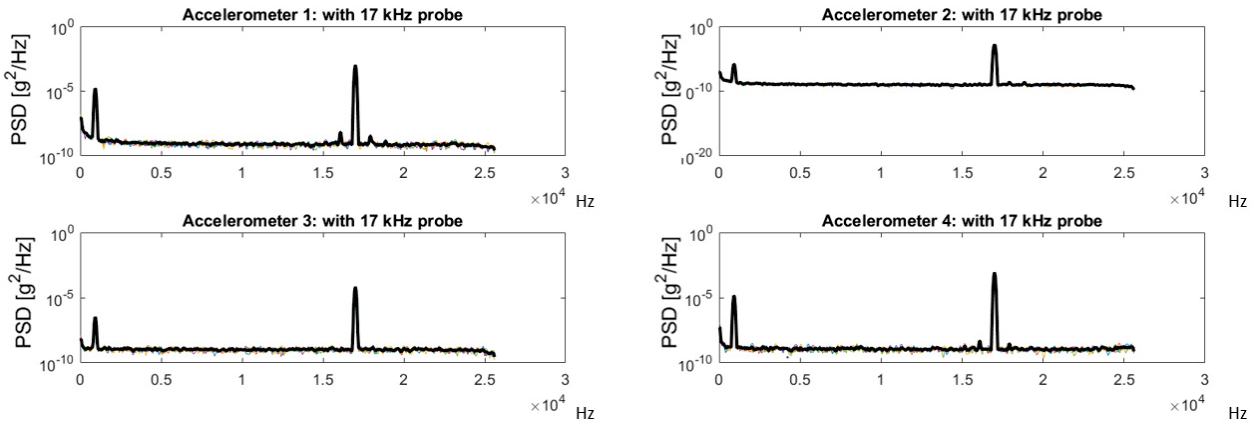

Figure 36. PSD plots for a 17-kHz probe and a 920-Hz pump in the locations noted in Figure 31.

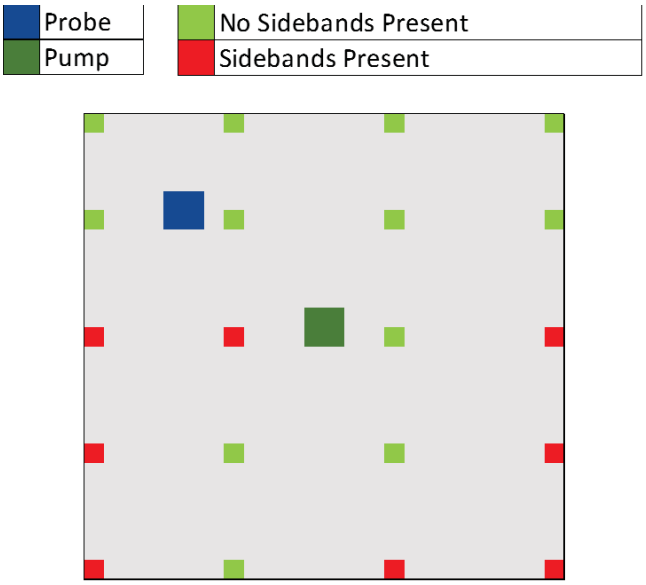

Figure 37. Sideband detection for 18-kHz probing and 920-Hz pumping frequencies.

Table 9. VAM results for Figure 34 (1: sidebands present; 0: no sidebands; - : missing data).

Pump Location	Probe Location	Probe Amplitude (mV amps)	Probe Frequency (kHz)	Observation Points																			
				1	2	3	4	5	6	7	8	9	10	11	12	13	14	15	16	17	18	19	20
Above Center	Q1	500	15	1	1	1	1	1	1	0	1	1	1	0	1	1	0	0	0	0	0	0	0
			16	1	0	1	1	1	1	1	1	1	1	1	1	0	0	0	0	0	0	0	1
			17	1	0	0	1	1	0	0	1	1	0	0	1	0	0	0	0	0	0	0	0
			18	1	0	1	1	1	0	0	1	1	1	0	1	0	0	0	0	0	0	0	0
			19	1	0	0	0	1	0	0	1	1	1	0	1	0	0	0	0	1	0	0	1
			20	1	0	0	1	1	0	0	1	1	1	0	1	0	0	0	0	0	0	0	0
Q1	Above Center	500	15	0	0	0	0	0	0	-	0	0	0	0	0	0	0	-	0	0	0	0	0
			16	0	0	0	0	0	0	-	0	0	0	0	0	0	0	-	0	0	0	0	0
			17	0	0	0	0	0	0	-	0	0	0	0	0	0	0	-	0	0	0	0	0
			18	0	0	0	0	0	0	-	0	0	0	0	0	0	0	-	0	0	0	0	0
			19	0	0	0	0	0	0	-	0	0	0	0	0	0	0	-	0	0	0	0	0
			20	0	0	0	0	0	0	-	1	0	0	0	1	1	1	-	0	1	1	0	0

4.3.3 Summary of VAM Results

Vibro-acoustic modulation successfully detected the damage in the structure. The above results summarize the experimental work conducted with respected to localization of the damage. Results so far show that the occurrence of sidebands is dependent on the pump and probe location, amplitude, and frequency. Through tuning of the experimental variables, the number of locations where the sidebands were detected can be narrowed by exciting the structure in only certain areas. The accelerometers that detected damage in the VAM experiments did not always correlate with the damage locations from the visible deformation locations in Section 3.2. However, the technique is showing promise, and future work will investigate the combination of computational modeling with experiments to further improve the damage localization.

4.4 Infrared Thermography

IR thermography measures the surface temperature of a structure and detects damage through variations in the recorded temperature over space and time. When a thermal load is applied to the structure, a damaged region will act as a discontinuity on the thermal load path – this will result in a

surface temperature above the damaged region that is different from undamaged regions. IR thermography can be used in a passive setting where heat comes naturally from the environment or in an active setting, as is the case here, where a user-defined heat load is applied to the specimen.

4.4.1 IR Thermography Test Setup

An IR thermographic camera is used to capture the temperature of the top surface of the concrete specimens. The IR camera has a resolution of 512x640 pixels, and its distance from the top of the medium concrete slab is adjusted to capture an image of the entire top surface of the specimen. The concrete slab is placed on top of a thermal heating blanket. The heating cycle for the blanket can be programmed based on specific applications. The heating blanket is also equipped with thermocouples to verify the temperature of the blanket. Since the slab has significantly more mass than concrete bricks (Mahadevan et al. 2016), a longer heating cycle was required to raise the temperature as seen in Figure 38.

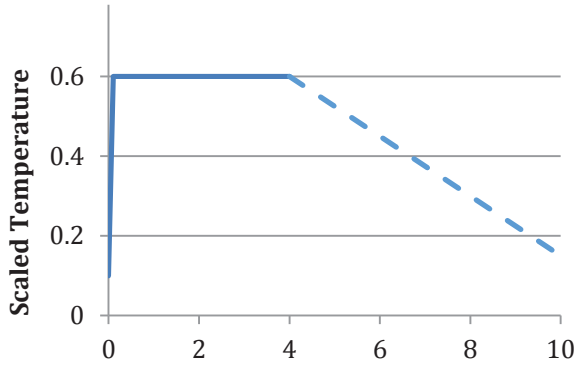

Figure 38. Heating blanket's temperatures cycle for the medium-sized concrete slab.

4.4.2 Analysis of Infrared Images

4.4.2.1 Temperature Measurement from IR Camera. For thermography imaging, a FLIR® IR camera is used to measure the surface temperature profile of the concrete specimen under investigation. The temperature measurements from an IR camera are verified by readings from five thermocouples installed on concrete samples at different locations (as shown in left image of Figure 39). The thermocouple temperature measurements are collected along with data from IR imaging measurements for verification purpose. Plots on the right of Figure 39 show temporal temperature profiles, which are measured by thermocouple (circle symbols) and IR-camera (solid line) at the Thermocouple 5 position for comparison. The two measurements are in suitable agreement at all five locations (similar to the plot on the right of Figure 39). Temperature measurement uncertainty using IR cameras is about 1–2% of measured temperature.

The first set of IR images was taken in about 1 week after casting, which can be used as the baseline temperatures, when slabs were considered fresh (or insignificant ASR gel exist). Then, depending on visual assessment of slabs' physical conditions the IR images were taken at time interval such that any change in the slabs' temperatures could be captured. At the beginning, images were taken weekly for bricks and every monthly for medium-sized concrete slab. Thus, changes in slab temperatures would indicate the impact of increasing ASR gel on the concrete temperature profiles.

4.4.2.2 Data Processing. Two data processing steps are applied to the acquired thermographic images: (1) image processing (extract data for areas of interest) and (2) calculating statistics (mean and variance) for each category classified by aggregate types and curing conditions. The results are used for observing any ASR induced temperature changes over time and impact of aggregates and curing methods on ASR progression. MATLAB® is used for this data processing and statistical analysis efforts.

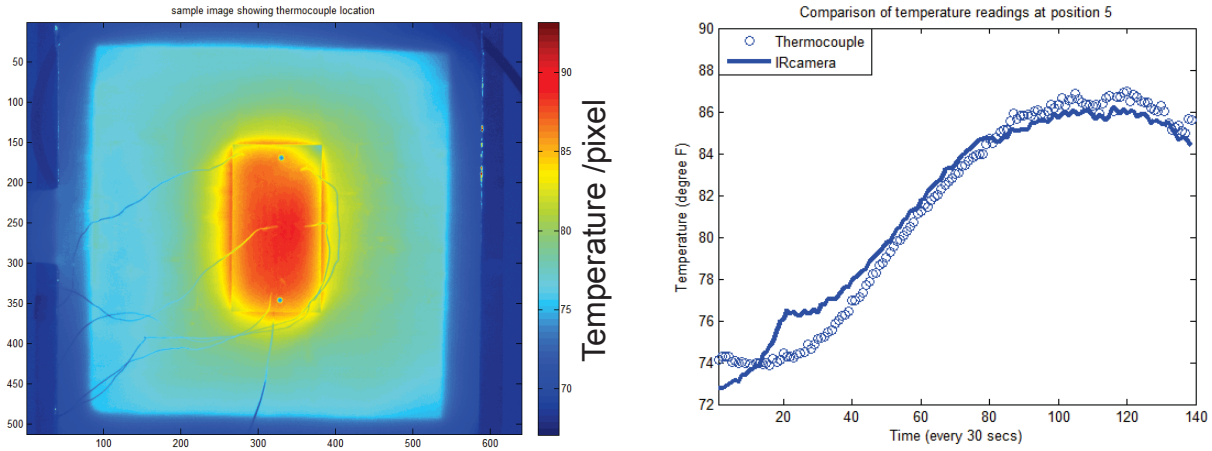

Figure 39. Thermal image of a brick sample showing five thermocouple locations (left) and plots of infrared-camera and thermocouple measurements at Position 5 as function of heating time (right).

Data extraction

The data extraction from IR images was done so that only data within the intended slab surface areas are used for analysis. The distinct dark blue areas outside of the slabs' surfaces in the left image of Figure 40 indicate lower outside temperature. This is a feature of the active IR thermography, when local heating increases contrast between heated object and surrounding areas. As a result, the locations of slabs are well defined within an IR image, as shown by the red rectangles in the left image of Figure 40. For the medium-sized concrete slab, each area of four different aggregate pockets can be extracted separately from corresponding quarter of the image as shown in the right image of Figure 40. Therefore, this allows temperature comparisons across different types of embedded aggregates and also across curing conditions as for the case of bricks.

Acquisition of thermographic images was performed over extended periods of time (more than 1 year for the medium-sized concrete slab) to capture changes in concrete temperature as the ASR gel is accumulating. It was impossible to keep the exact settings of camera and slab(s) locations, so captured images are slightly shifted across different data acquisition dates. Therefore, the extracted areas are taken well within the slab surfaces. For three bricks, data from three corresponding rectangular areas within each slab were extracted from each image frame as shown by red rectangles in the left image in Figure 40. For the medium-sized concrete slab, data of four 200 x 200 pixels areas corresponding to four aggregate quadrants of slab image staring from the center of were extracted, as shown in image on the right in Figure 40. The minimum temperatures from each extracted area were checked to make sure that no temperatures from outside (which are distinctively lower) are included in the analysis.

Statistical analysis

Basic statistics, *spatial mean and variance* (or square of standard deviation), are important characteristics representing slab temperature distribution. These statistical parameters characterize slab's spatial (or area) temperature distribution, which can be used to track changes over time for different slab

categories. For a fresh slab, temperatures are more spatially uniform as the structure is still homogeneous. As the ASR gel increases in volume and exerts an expansive pressure inside the material, causing spalling micro- to macro-cracks, it causes the concrete structure to become nonhomogeneous due to non-uniform moisture distribution. This effect leads to changes in slab temperature distribution. The use of the spatial mean (or area average) values allows limiting effect of measurement noise (or uncertainty), which is about 1–2% of measured temperature. The ASR-induced change in temperature profile could be small, which can be overlooked by measurement noise. Change in average temperature indicates overall impact of ASR

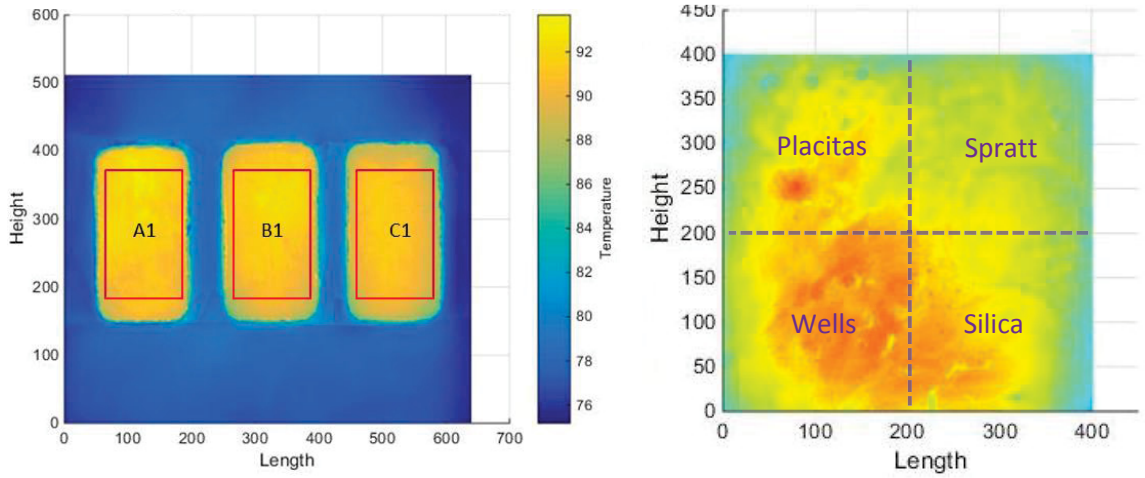

Figure 40. Thermal images of three bricks (left) and a medium-sized concrete slab (right).

product on slab temperature. On the other hand, ASR-induced nonhomogeneous structure of concrete creates discontinuity of thermal paths, which could lead to a greater variation of the slab's temperature throughout its structure. Therefore, temperature spatial variation can be used to observe slab temperature change, subsequently assessing the extent of ASR progression. *Area-average temperature* (T_{Ave}) for an extracted area of interest is expressed as:

$$T_{Ave} = \frac{\sum_{i=1}^{N} T_i}{N} \quad (1)$$

Temperature *variance* (T_{Var}) for an area of interest can be calculated as a square of *standard deviation* of temperature distribution as:

$$T_{Var} = \frac{\sum_{i=1}^{N} (T_i - T_{Ave})^2}{N-1} \quad (2)$$

where T_i is the temperature at i pixel and N is the number of pixels within the extracted area.

Figure 41 shows area-average temperatures as function of heating time for four different aggregate areas of the medium-sized concrete slab. At the beginning of the heating cycle, slab temperatures are at room temperature, which vary in the range of 70 to 75˚F over 1 year of image acquisition period. This variation of the initial room temperature is excluded from the temperature temporal profile to accurately capture the change in the slab's temperature over time due to possible ASR-induced change in material thermal conductivity. Therefore, only temperature increase from room temperature during the heating cycle is used to assess temperature changes across data acquisition dates.

Temporal temperature gradient (as degrees (F) per minute), which represents concrete thermal conductivity, could also be used to observe the extent of ASR progression. This is because the presence of

ASR gel is believed to cause change in concrete thermal conductivity. This temperature gradient can be calculated using temperature from two consecutive frames as follows:

$$\Delta T = (T_i^{Avg/Max} - T_{i-1}^{Avg/Max})/dt, \quad (3)$$

where $T_i^{Avg/Max}$ and $T_{i-1}^{Avg/Max}$ are either average or maximum temperature of the Frames i and $i-1$, respectively; and *dt* is the time between two consecutive frames. The temperature gradients are smoothed as an averaged value from eight frame intervals. The temperature gradients are used to access the rate of change in slab surface temperature over heating time, which is directly related to the slab thermal conductivity.

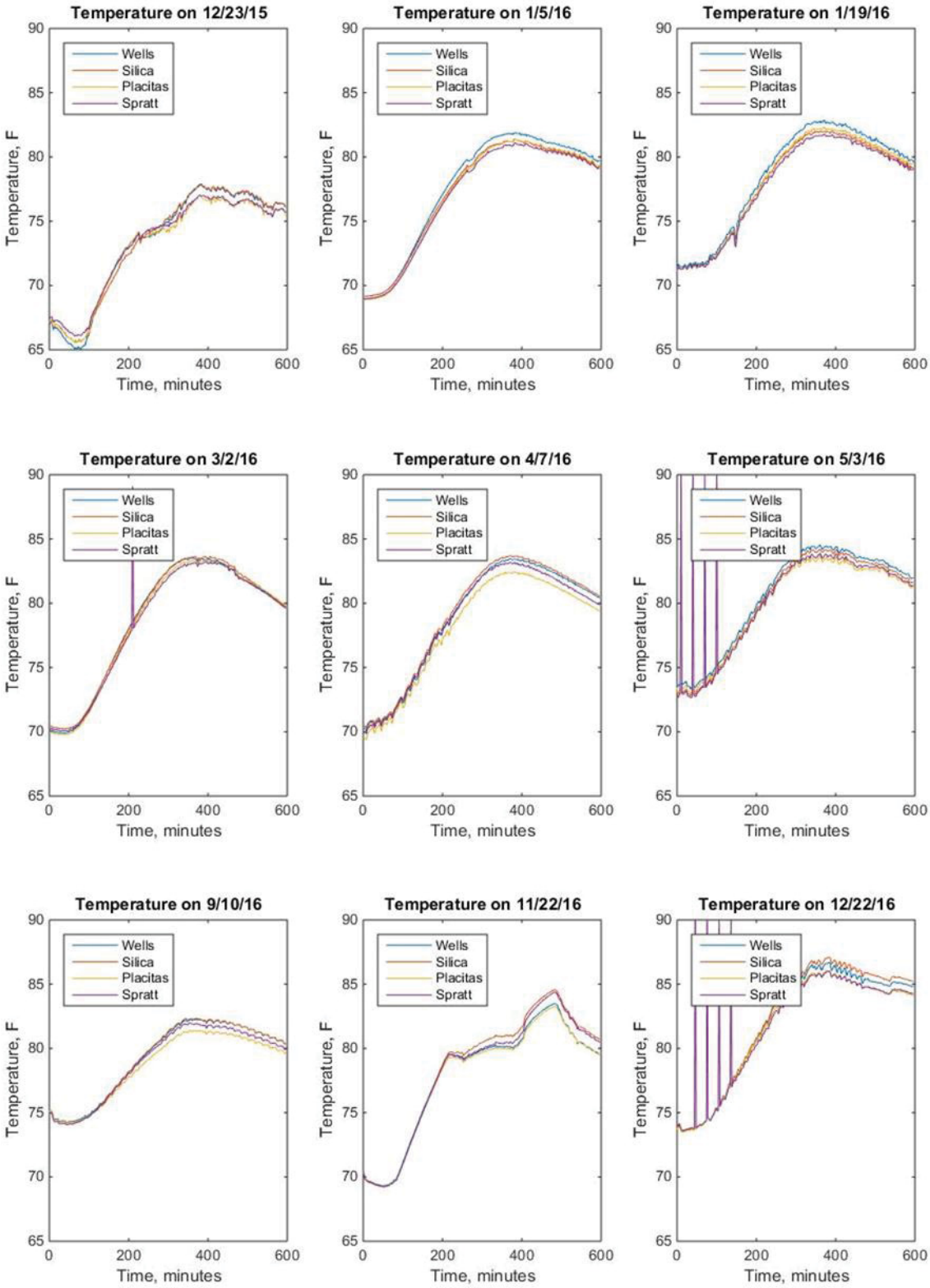

Figure 41. Area-average temperatures as function of heating time for four aggregate pockets.

4.4.3 Results for Cement Bricks

For each set of three bricks, the IR images were taken every 30 seconds during the entire 140-minute heating cycle. However, images for the first 70 minutes during the first heating period were analyzed to assess the impact of ASR gel formation on the concrete temperature profiles. The highest temperatures during the first heating cycle, peaked at 60 minutes after the onset of the heating (at start of the subsequent cooling down period). Eight data sets of IR images for bricks were acquired during time period between August 17 and October 8, 2015. Visible changes in the bricks' structural conditions were observed on September 30, 2015 (see Mahadevan et al., 2016), so the IR images of these bricks were taken every day or every other day to observe if any changes in brick temperature profile have occurred.

4.4.3.1 Thermographic Images. The thermographic images in Figure 42 show cropped areas of the three bricks within a frame of the IR image taken at 1 hour after the onset of the heating cycle (when the slabs' temperatures were near the peak) for various date during about a yearlong of experiment. These images are extracted from the Frame 120 for each data acquisition date. The one color bar is used represent temperature increase relative to the temperature at the start of heating cycle for all dates, so temperature change over time can be observed. Following observations can be seen from these images:

- The color shapes are fairly consistent (without much higher temperatures of background) for all images taken at different dates indicating that the cropped areas are actually representing four locations of aggregate pockets.
- For each date, temperatures for the one slab's surface vary within a quite small range [min–max] of about 4°F, which is only slightly more than measurement uncertainty of 1–2% of temperature readings.

4.4.3.2 Area-Average Temperature, Variance, and Gradient. Figure 43 shows temperature increases. Figure 44 shows temperature variances, and Figure 45 shows temperature gradients as function of time for one heating cycle and all image acquisition dates. For four aggregate areas, Figure 46 shows the highest area-average temperature during the first heating period within a cycle for water curing on the left-hand side and for NaOH solution curing on the right hand side as function of image date. This plot can be used to assess impact of ASR progression over time. For assessing impact of curing methods, Figure 47 shows the peak area-average temperatures for each slab with two curing methods together as function of image date. Finally, effect of two glass aggregates (B and C) can be seen in Figure 48, which depicts plots of differences in temperature increases from the cement-only slab (A) for two curing methods, separately. Following observations can be seen:

- For each date, average temperature increases for three slabs are quite similar to each other, but overall temperature changes over image date can be seen in Figure 43.
- Temperature variances in Figure 44 are less than 1.5˚F for three slabs and all image dates, which are similar to thermographic temperature measurement uncertainty. This indicates that ASR-induced temperature change for one slab is insignificant. This consistency in temperature variances indicates the fact that extracted (cropped) areas are actually representing all three brick surfaces.
- Temperature gradients in Figure 45 shows that temperature of brick increased at the rate up to 0.5˚F per minute) during heating cycle. The negative gradients after 60 minutes of heating indicate that the slabs started to cool down after the first period of heating.
- For water curing slabs, peak (highest) temperatures as function of image dates in plot on the right of Figure 46 show that the slabs' temperature started to increase from October 5 to October 8 for water curing slabs. However, the increase was little and only for a short 3 days, so it is not a clear increasing trend. For NaOH curing slabs (right plots), there is no trend of temperature change over time apparent.
- Figure 47 show, only to some extent, a downward trend for the aggregate from the wells. The other two aggregates have slightly lower temperatures than silica.

- For temperature differences relative to Slab A (Figure 48), Slab B shows no trend over time, but Slab C shows a clear upward trend of temperature differences.

In summary, ASR-induced temperature changes measured by the IR thermographic method is able to detect some changes in temperature for bricks.

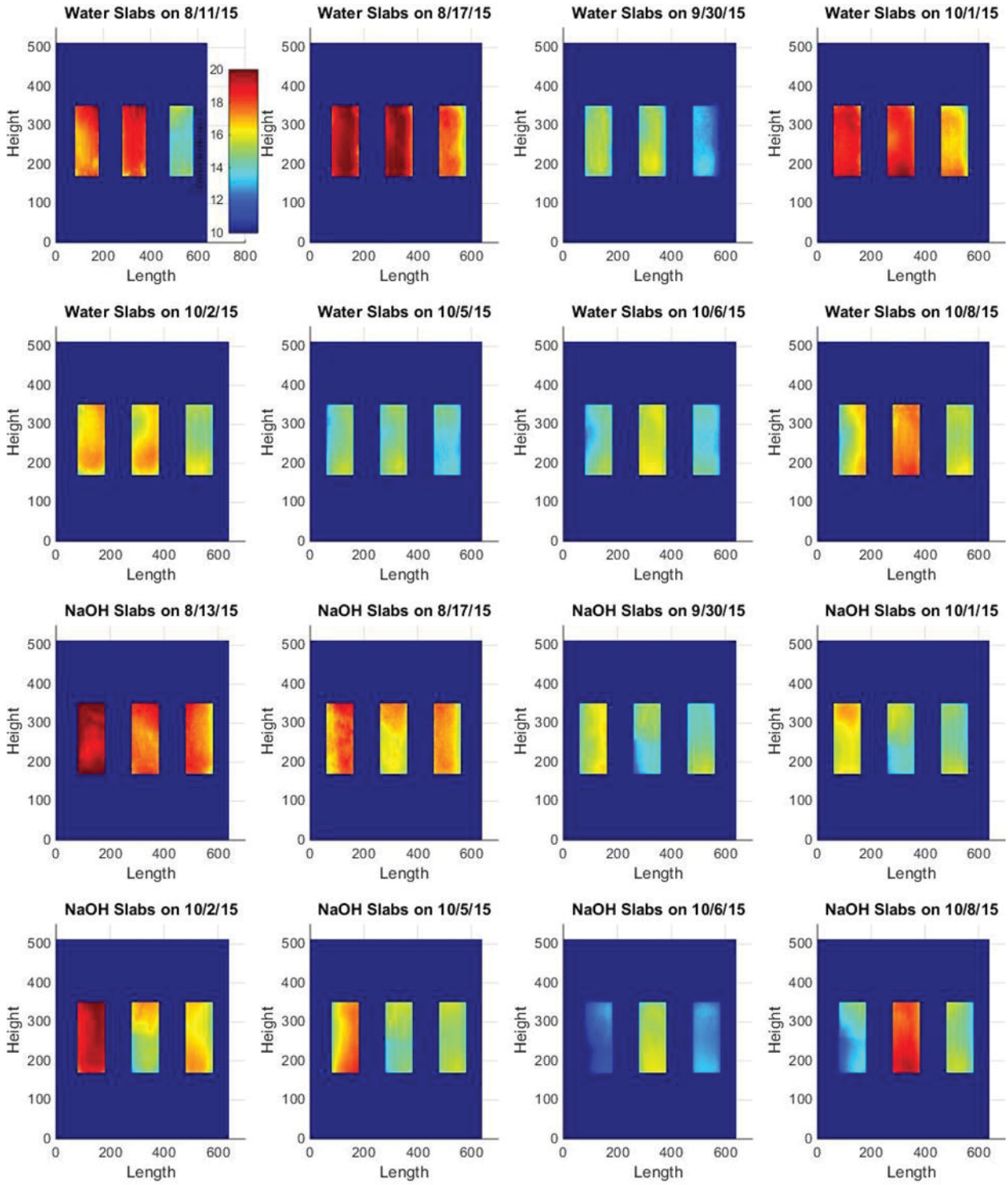

Figure 42. Thermographic images of three slabs temperature increase relative to room temperature at 1 hour into the heating cycle taken at different dates from August 13, 2015 to October 8, 2015.

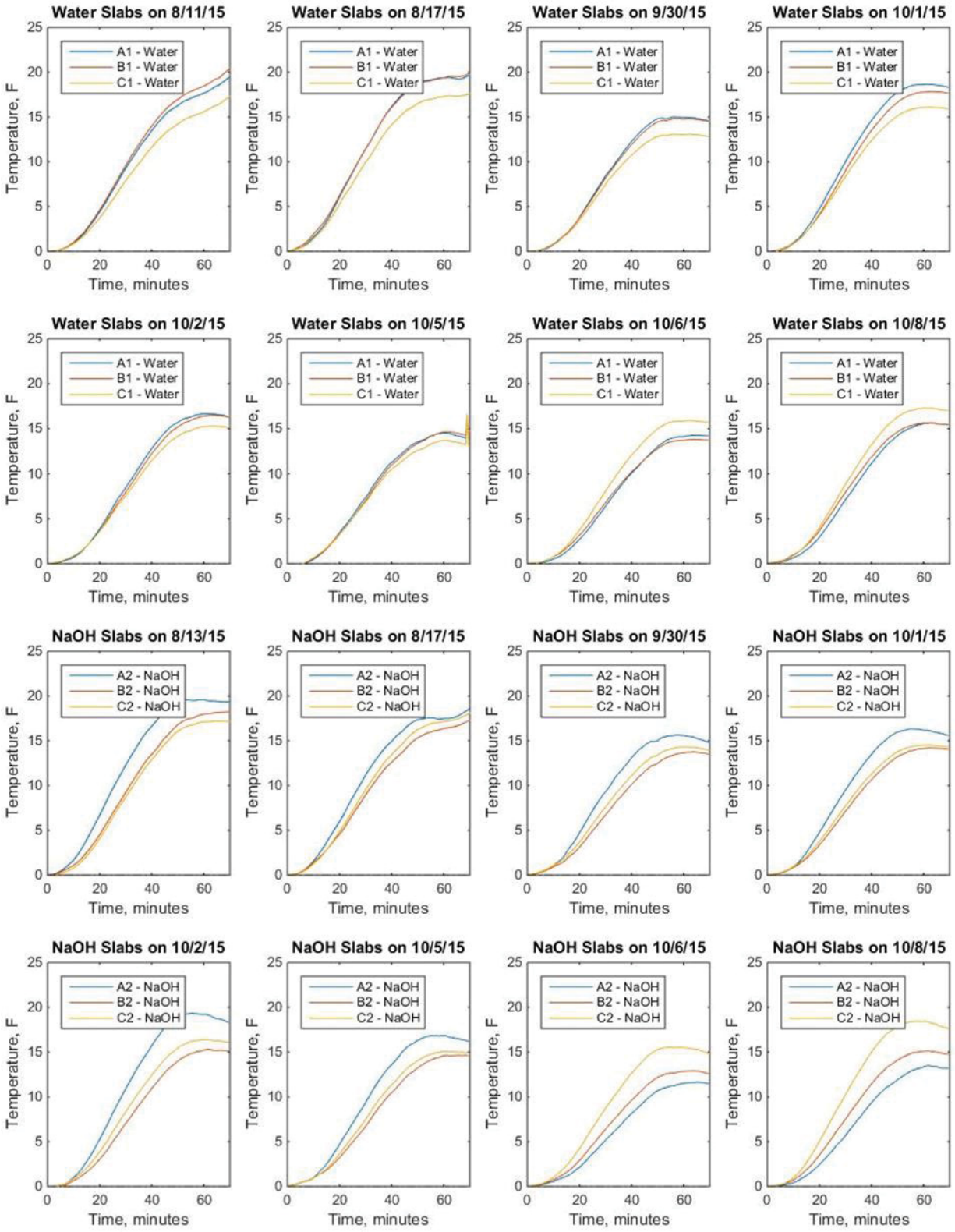

Figure 43. Area-average temperature increases of three bricks at different acquisition dates from August 13, 2015 to October 8, 2015.

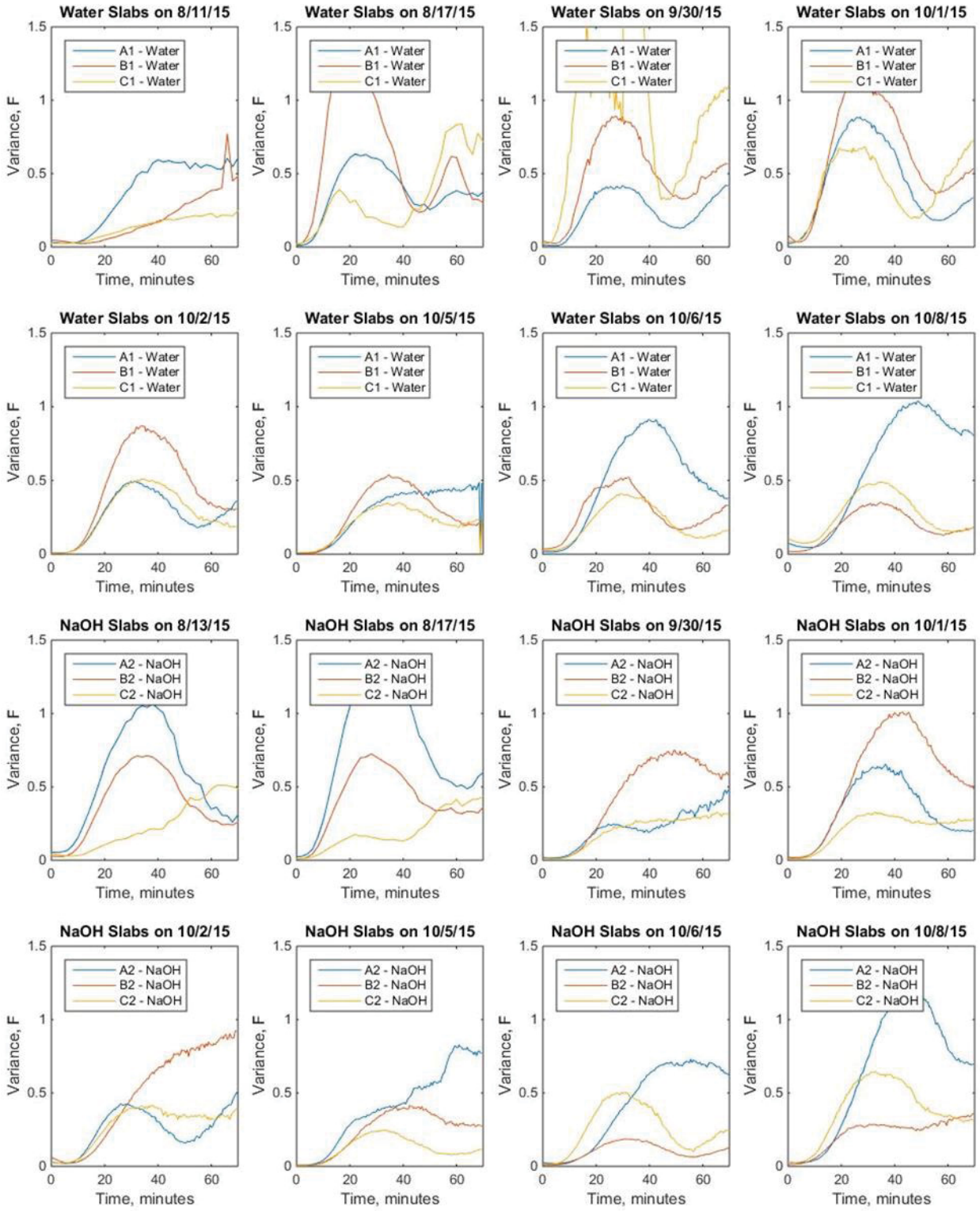

Figure 44. Area-average temperature variances of three small bricks at different acquisition dates from August 13, 2015 to October 8, 2015.

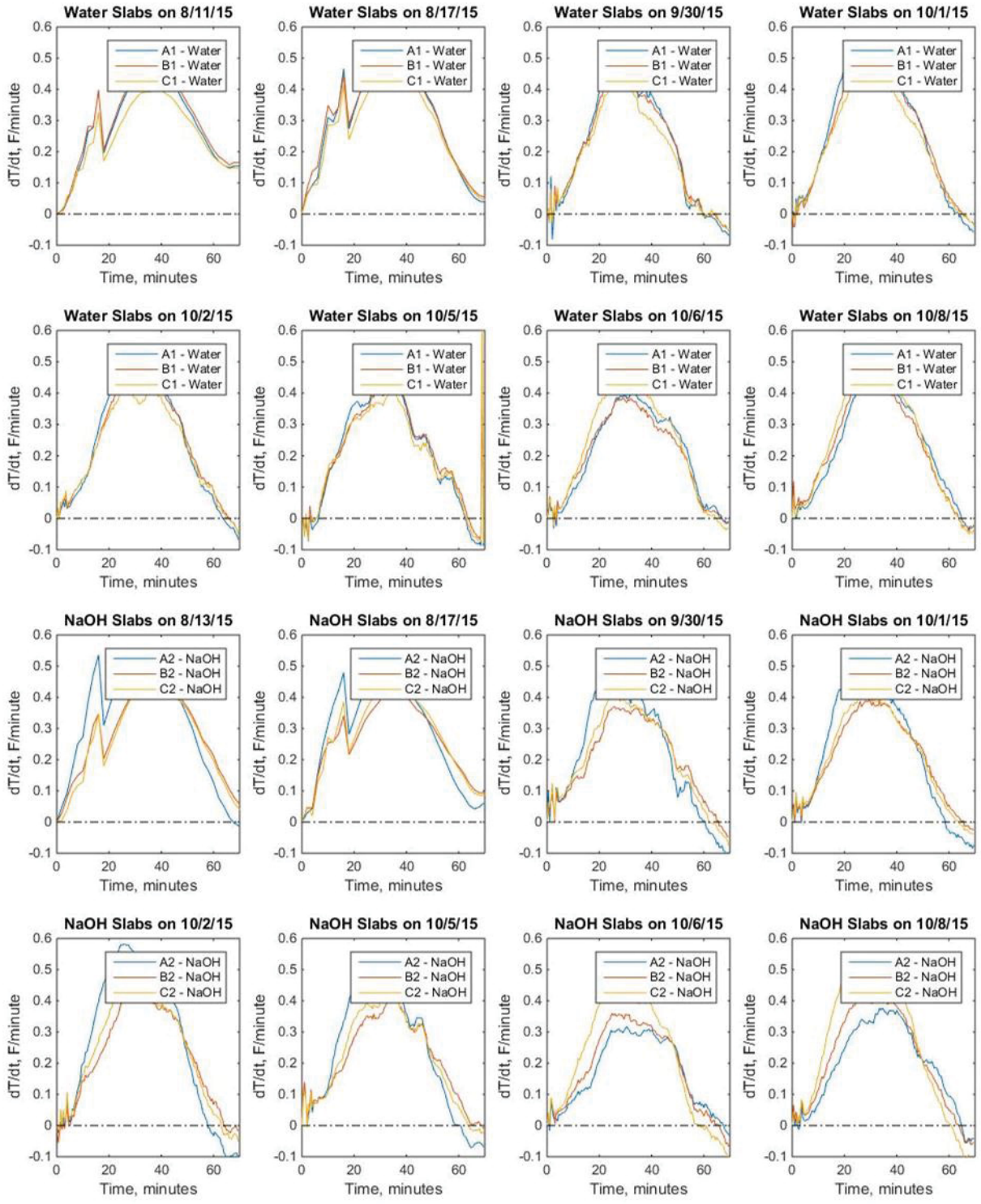

Figure 45. Area-average temperature gradients of three bricks at different acquisition dates from August 13, 2015 to October 8, 2015.

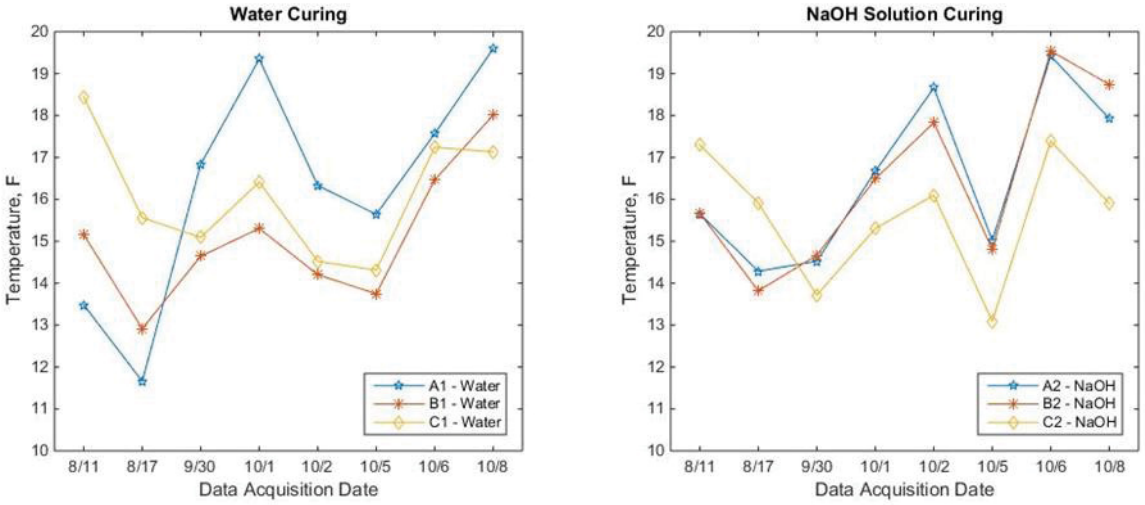

Figure 46. First peak of area-average temperature increase for water curing (left) and NaOH curing (right) for three bricks as function of image date.

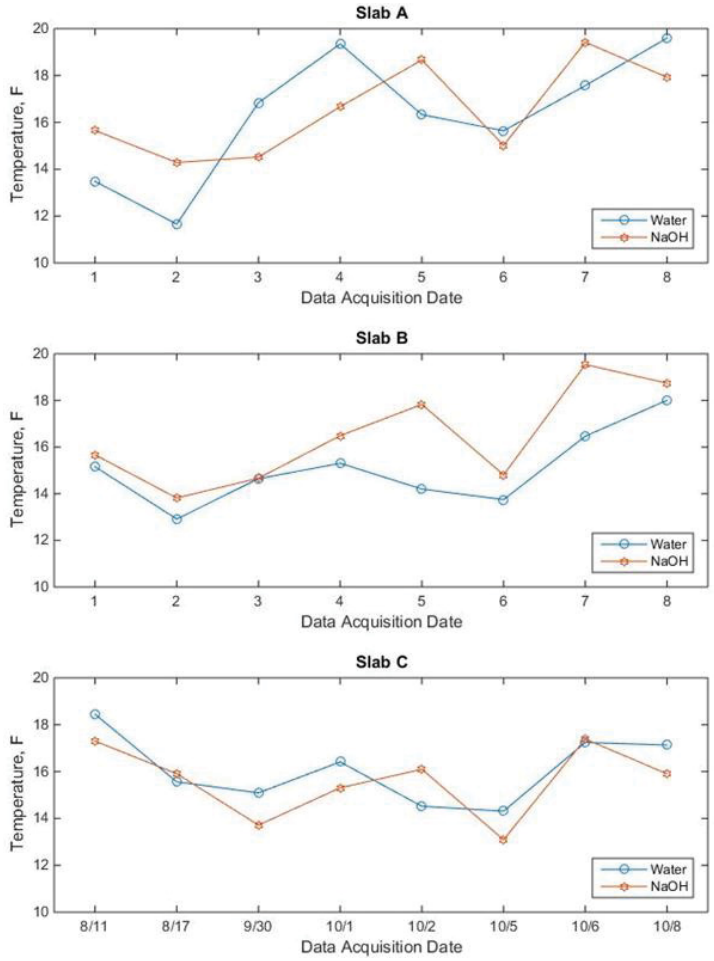

Figure 47. First peak of area-average temperature increase for three bricks as function of image date for curing method comparison.

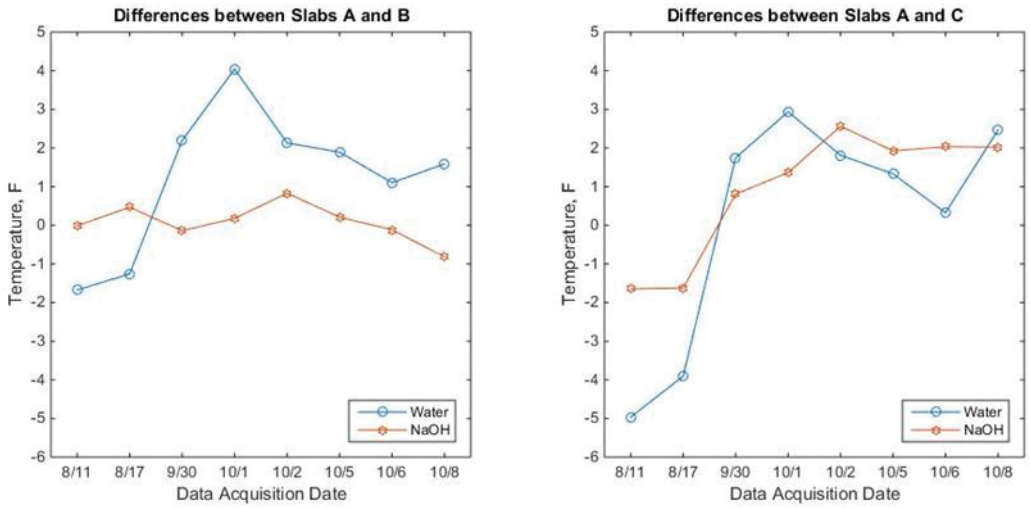

Figure 48. Area-average temperature difference from Slab A (cement only) as function of image date.

4.4.4 Results for Medium-Sized Concrete Slab

4.4.4.1 Thermographic Images. Thermographic images in Figure 49 show a cropped central area of the medium-sized concrete slab taken at various date during about a yearlong of experiment. Each aggregate pocket is located in one quadrant of an image as shown in Figure 40. These images are extracted from the Frame 150 (after 5 hours of heating) for each data acquisition date. The one color bar represents temperature increases relative to temperature at the start of heating cycle for all dates so that temperature change over time can be observed. Following observations can be seen from these images:

- The color shapes are fairly consistent for all images taken at different dates indicating that the cropped areas are actually representing four locations of aggregate pockets
- For each date, temperatures for the entire slab's surface vary within a quite small range [min–max] of about 4°F, which is only slightly more than measurement uncertainty of 1–2% of temperature readings. Since the temperature differences between aggregate areas should be smaller than that range, it could be difficult to identify.
- Even though there are significant differences in temperatures across dates, but there is no clear trend in temperature changes over time–the highest temperature increases were on March 2, 2016 and the lowest were on the later date, September 10, 2016.

4.4.4.2 Area-Average Temperature, Variance, and Gradient. Figure 50 shows temperature increases, Figure 51 shows temperature variances, and Figure 52 shows temperature gradients as function of time for one heating cycle and all image acquisition dates. For four aggregate areas, Figure 53 shows highest area-average temperature during a heating cycle (plots on the left) and highest variances as function of image date (plots on the right). For assessing impact of aggregates on ASR-induced temperature changes, Figure 54 shows the area-average temperature differences relative to silica aggregate temperature as function of image date. Following observations can be seen:

- For each date, average temperature increases for the four aggregate areas are quite similar to each other with very insignificant variation across aggregate types.
- Temperature increases during a heating cycle were abnormally low on September 10, 2016 and irregular on November 22, 2016. The higher resolution camera was used for both dates. In addition, the temperature variances are also notably lower during dates when the new camera was used (from April 2016) as shown in Figure 51. This difference in cameras could influence on findings temperature changes.

- Temperature variances in Figure 51 are less than 1.5°F for four aggregates and all image dates, which are similar to thermographic temperature measurement uncertainty. This indicates that ASR-induced temperature change is insignificant and the measurement method is not sensitive enough for detecting ASR progression.
- Temperature gradients in Figure 52 shows that temperature of medium-sized concrete slab increased very slowly (generally less than 0.1°F per minute) during heating cycle. This indicates very low thermal conductivity of slab material.
- The peak temperatures and variances as function of image dates in Figure 53 confirm that there is no trend in temperature changes over time for all four aggregates. Also, differences in the two cameras used for medium-sized concrete slab experiment are noticeable by consistently smaller variances from the new higher resolution camera (from April 2016).
- Temperature changes relative to Silica aggregate presented in Figure 54 show, only to some extent, a downward trend for the aggregate from Wells. Other two aggregates have slightly lower temperatures than silica.

In summary, ASR-induced temperature changes measured by the IR thermographic method is insignificant for the medium-sized slab. Thus this method sensitivity is not enough for detecting impact of ASR progression on material thermal conductivity for medium-sized concrete slab due to the longer time to heat it.

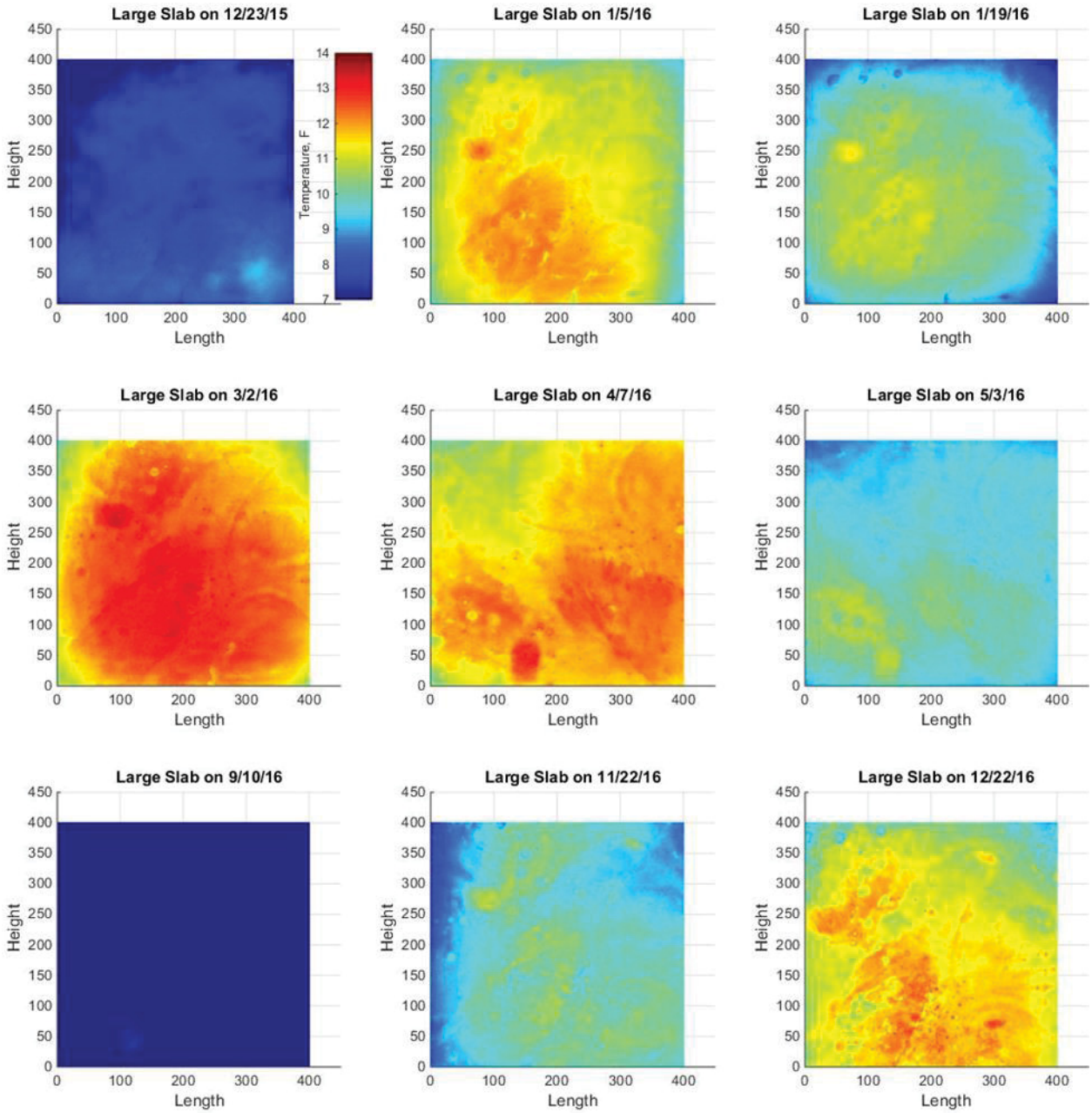

Figure 49. Thermographic images of the medium-sized concrete slab temperature increase relative to room temperature at 5 hours into the heating cycle taken at different dates from December 13, 2015, to December 22, 2016.

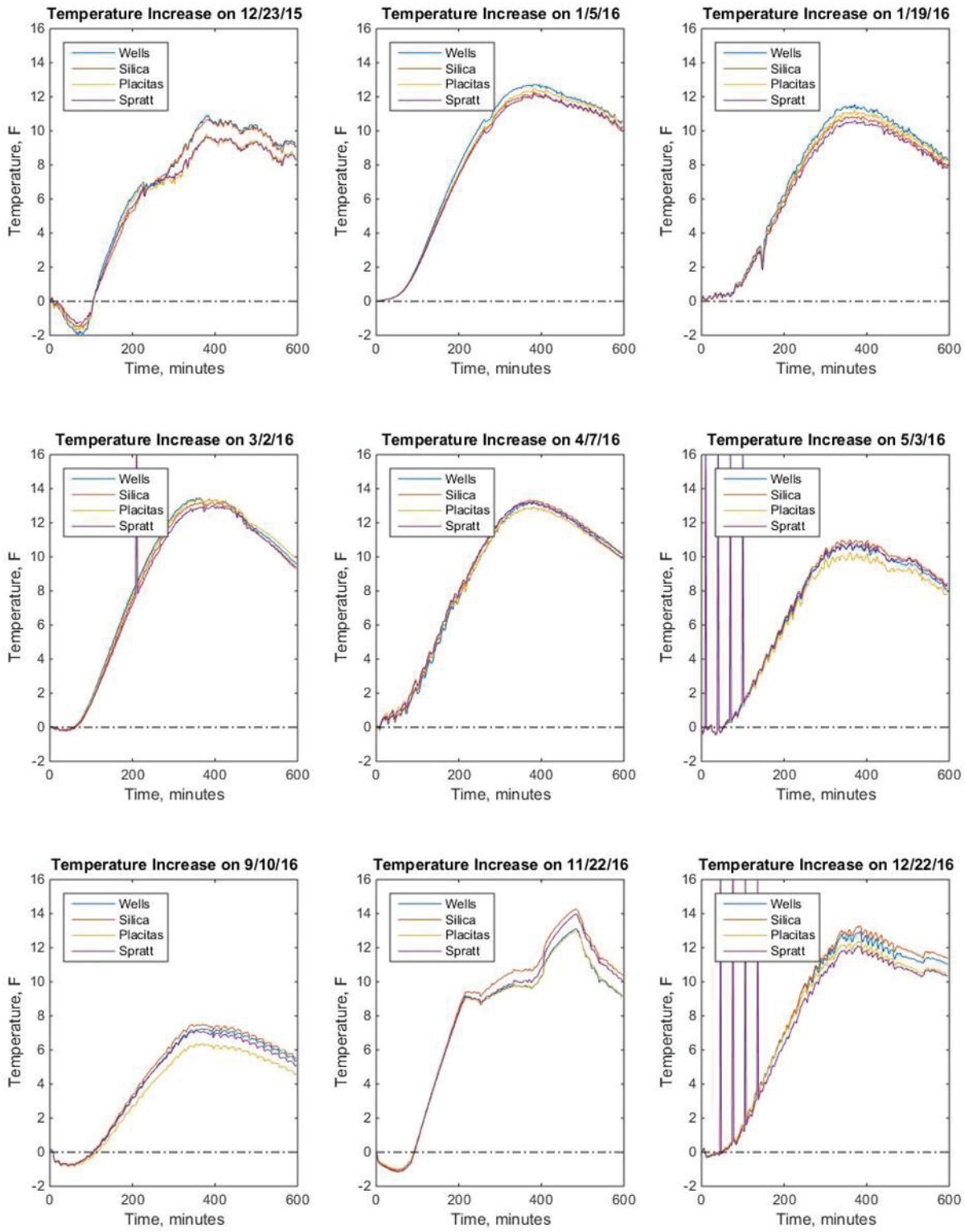

Figure 50. Area-average temperature increases of four aggregate pocket areas in the medium-sized concrete slab at different acquisition dates from December 13, 2015, to December 22, 2016.

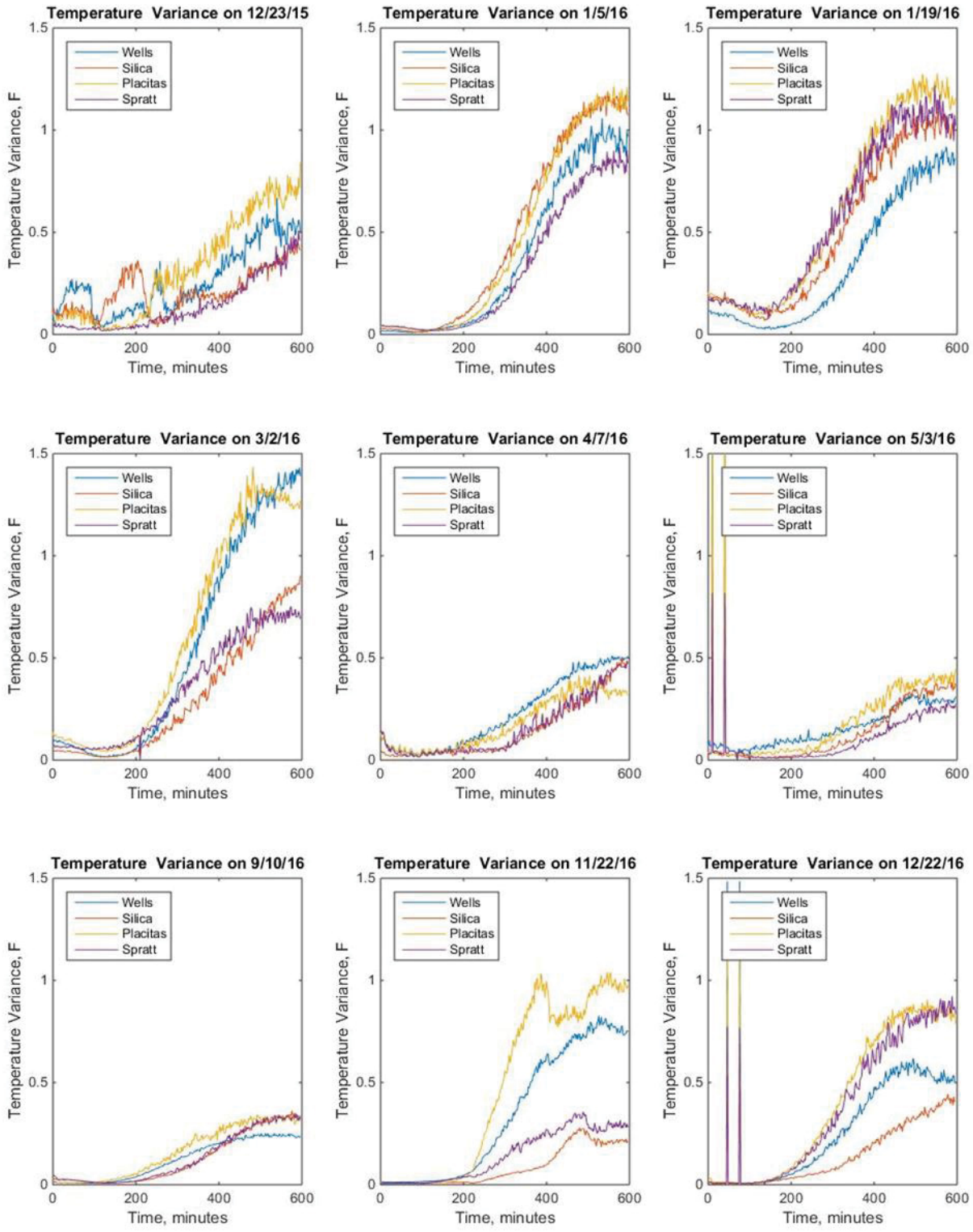

Figure 51. Temperature variances for four aggregate areas in medium-sized concrete slab at different acquisition dates from December 13, 2015, to December 22, 2016.

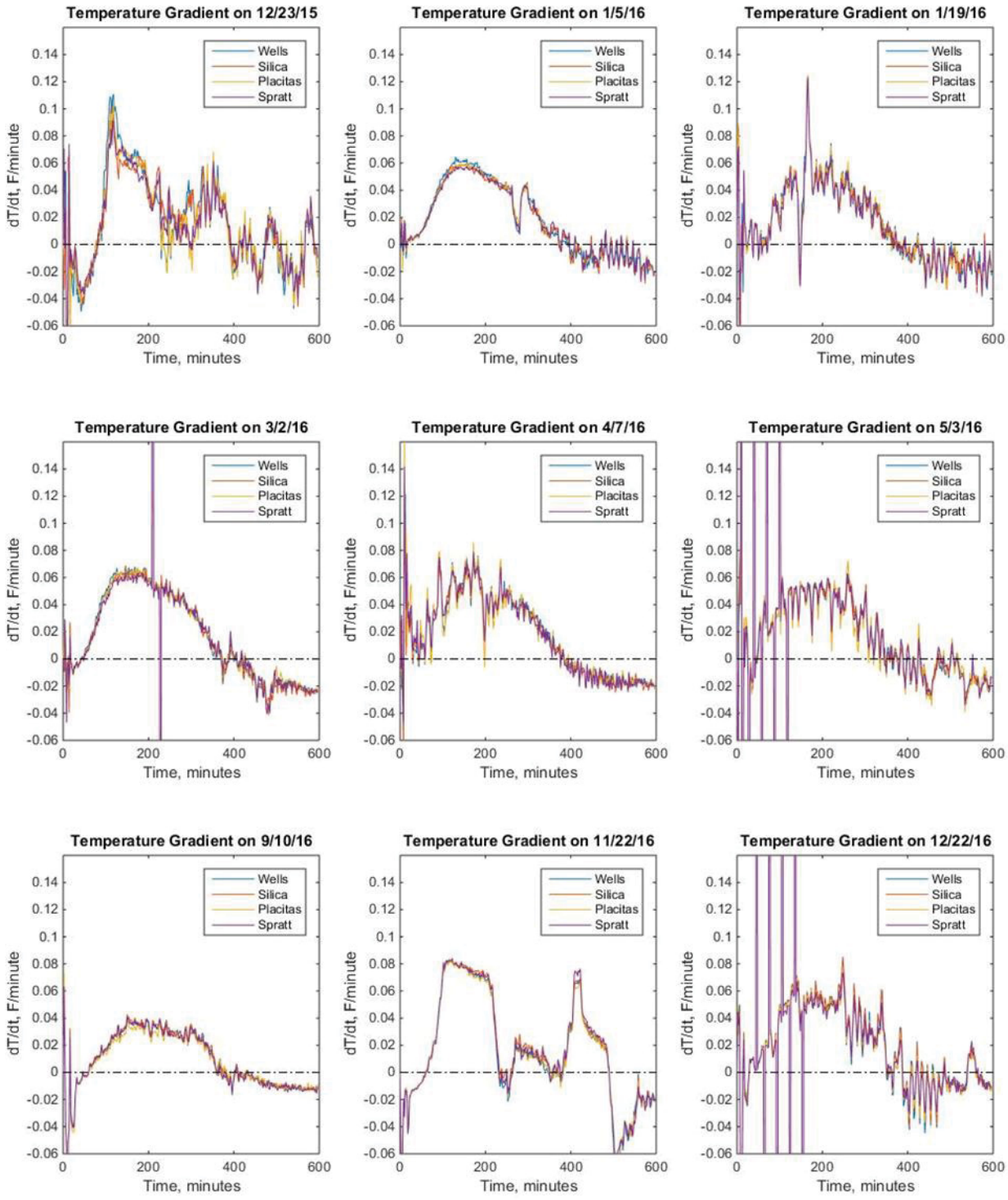

Figure 52. Area-average temperature gradients of four aggregate pocket areas in the medium-sized concrete slab at different acquisition dates from December 13, 2015, to December 22, 2016.

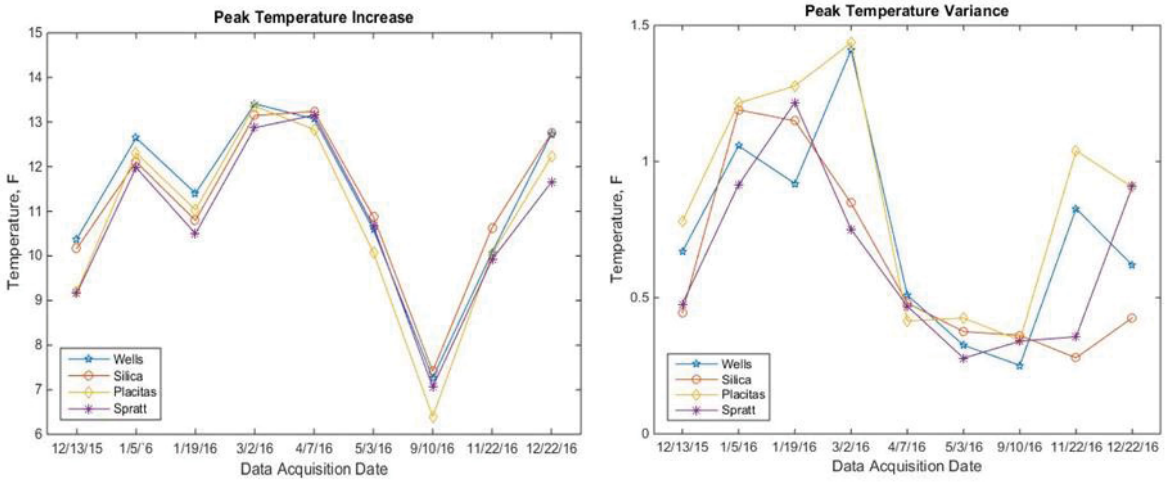

Figure 53. Peak area-average temperature increase (left) and variance (right) for four aggregate areas as function of image date.

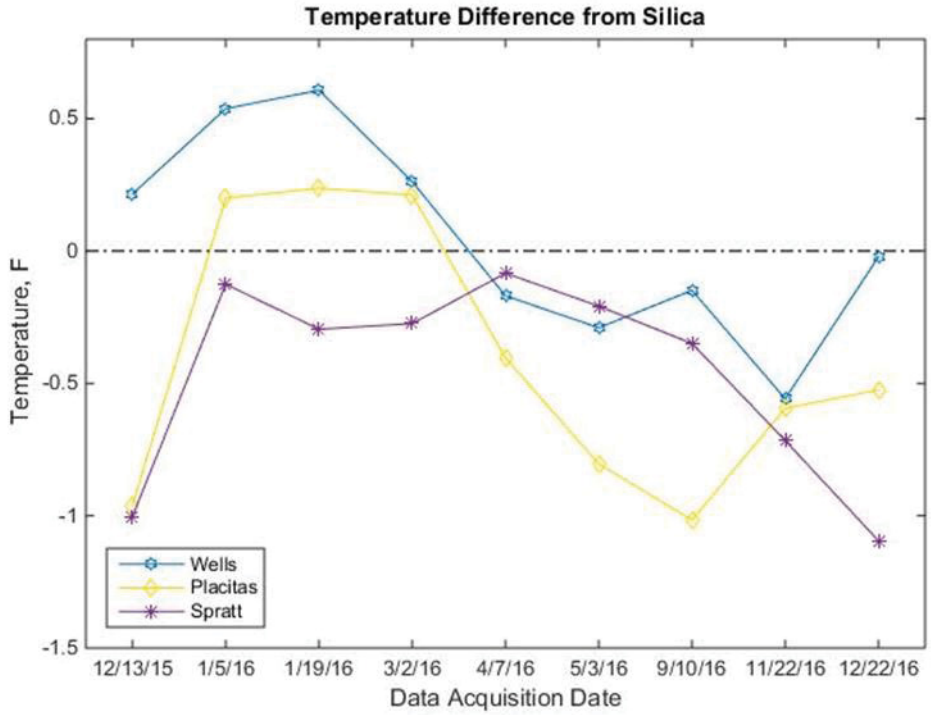

Figure 54. Area-average temperature difference from silica aggregate as function of date.

4.5 Digital Image Correlation

The DIC technique was applied to the large concrete slab cast at the University of Tennessee, Knoxville. DIC is a three-dimensional, full-field, optical NDE technique to measure contour, deformation, vibration, and strain. The technique can be used for many tests, including tensile, torsion, bending, and combined loading for both static and dynamics applications.

4.5.1 DIC Test Setup

An experimental setup for three-dimensional DIC and data analysis includes following steps:

1. Preparation: Two cameras are mounted at either end of a tripod camera (base) bar so the relative position and orientation of the two cameras with respect to each other is known. A random or regular pattern with good contrast is applied to the surface of the test object. The initial imaging processing defines unique correlation areas, known as facets, that are defined across the entire imaging area and that typically range in size from 5 to 20 square pixels.
2. Data acquisition and processing: An image correlation algorithm tracks the movement of these facets by utilizing mathematical methods to maximize the similarity measures from successive images. The three-dimensional locations of each facet can be calculated. Full-field displacement data can be obtained by tracking these measurement facet points within the applied random (or regular) target pattern.
3. Results: Out-of-plane displacement (or deformation) map for the entire surface for each point in time, when the measurements are taken. Progression of expansion or relaxation of structure affected by various degradation mechanisms including the ASR, which can be calculated using the displacement maps taken at different times during the testing period or long-term operation.

As part of the inter-pathway collaboration within the Light Water Research Sustainability Program, Vanderbilt University is conducting research to investigate the monitoring of degradation in concrete sample at the University of Tennessee - Knoxville due to an ASR using the DIC techniques. Vanderbilt University began performing DIC in late August 2016 on an ASR mockup concrete slab at the University of Tennessee, Knoxville. Three slabs were cast and the progression of the ASR will be studied over 3 years with a variety of monitoring techniques. A black-background-white-speckle pattern using acrylic latex paint was selected and applied to the slab. At the same time, the supporting fixtures for the DIC camera were also installed inside the environmental chamber. Technical basis for selecting optimal experimental settings were discussed in the Neal et al. 2016.

One of the three slabs was allocated for monitoring using DIC, on a 2 ft x 2 ft square area on the top surface. The side view of the slab inside an environmental chamber is shown in Figure 55 and the DIC camera is shown in Figure 56. For DIC monitoring effort, a preliminary study was performed to determine the optimal speckle size and pattern and identify the most durable paints (Neal et al. 2016).

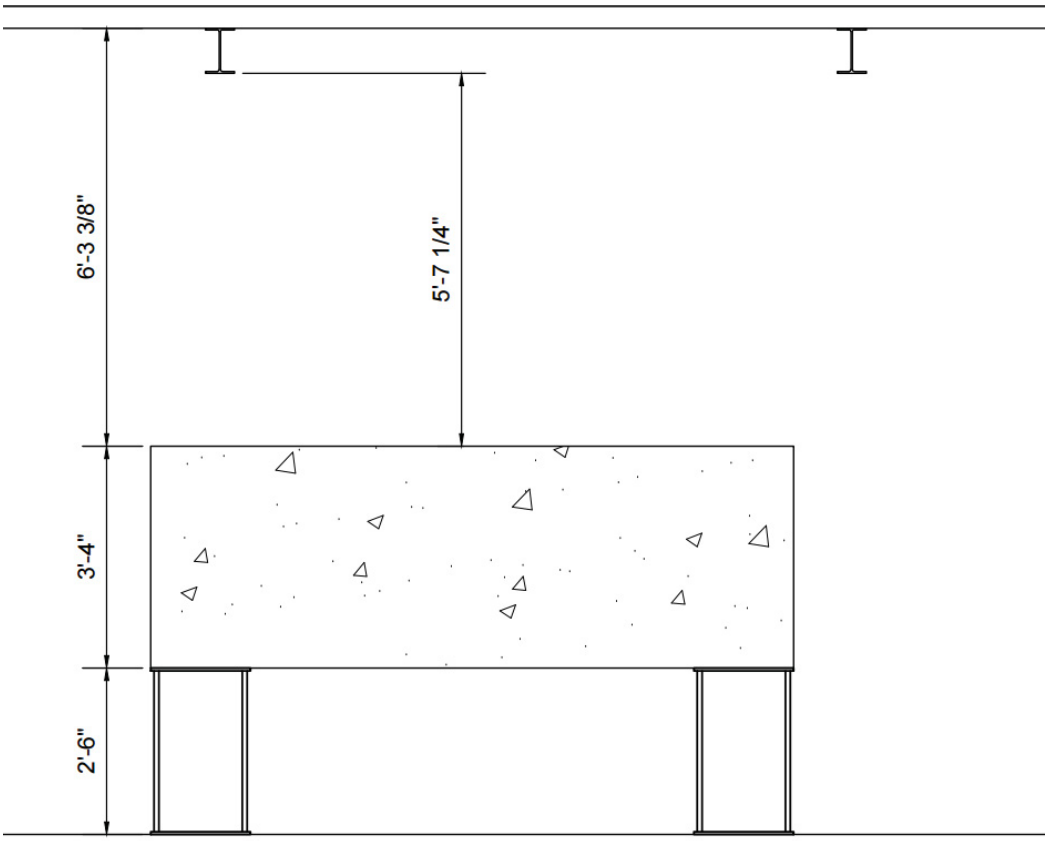

Figure 55. Side view of the slab at the University of Tennessee.

Figure 56. DIC camera support installation over the area of interest.

4.5.2 DIC Results

The large mock-up slab at the University of Tennessee, Knoxville was studied using the DIC technique, every 2 months. The DIC results, namely strain distributions in the X and Y directions (along with the dates), are shown in Figure 57 and Figure 58, respectively. Figure 57 and Figure 58 show that DIC is effective in capturing the strain due to deformation in the large slab, caused by expansion with time. In addition, the color bars on the right of each image indicate the strain values corresponding to different colors, and also the frequency distribution of the strain values. Thus in Figure 57, the normal strain in the X direction was zero everywhere in August 2016, then the average value increased to approximately 1150 μm/m in October 2016, and to approximately 1950 μm/m in February 2017. Similarly in Figure 58, the normal strain in the Y direction was zero everywhere in August 2016, and then the average value increased to approximately 1250 μm/m in October 2016, and to approximately 2250 μm/m in February 2017. These results indicate that the large slab experienced significant expansion during the period from August 2016 to February 2017. Two issues were noted: (1) the data collected in December 2016 was unusable due to instrument malfunction; and (2) some damage to the speckle pattern was observed, as indicated by the white spots on the right hand side of the diagonal (the white spots along the diagonal indicate the studs placed for visual measurement of deformation). The cause for the damage is suspected to be caused during the conduct of other NDE experiments on the slab. However, the damage has not affected the DIC results; the overall strain distribution is of importance and it is well captured by Figure 57 and Figure 58.

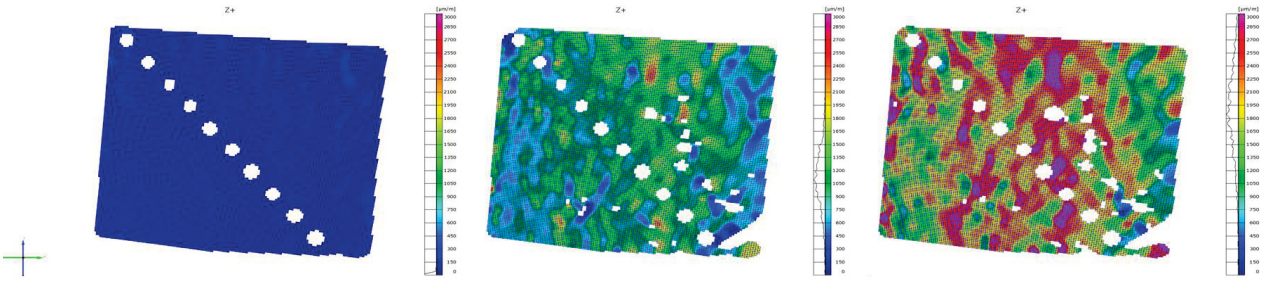

First measurement (Aug. 8, 2016) – S1 | Second Measurement (Oct 17, 2016) – S11 | Fourth Measurement (Feb. 2, 2017) – S31

Figure 57. Strain distribution (Normal strain in the X direction).

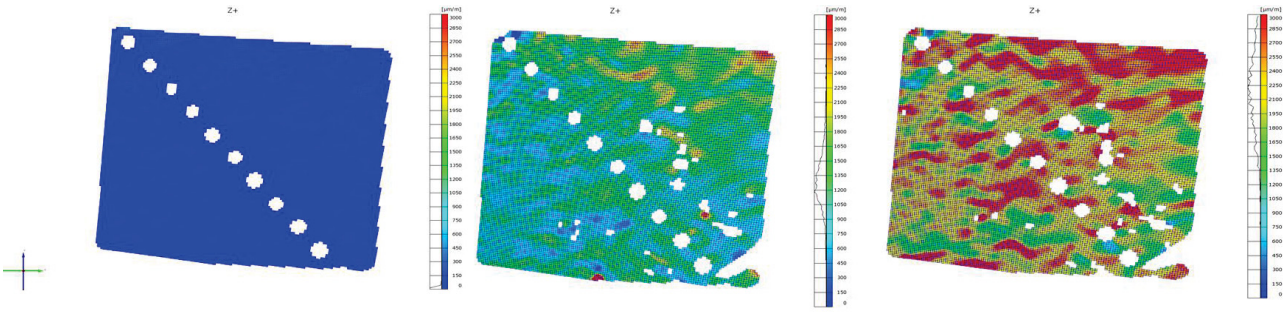

First measurement (Aug. 8, 2016) – S1 | Second Measurement (Oct 17, 2016) – S11 | Fourth Measurement (Feb. 17, 2017) – S31

Figure 58. Strain distribution (Normal strain in the Y direction).

5. SUMMARY AND FUTURE WORK

The objective of this report was to examine the application of NDE techniques (thermography, mechanical deformation measurements, NIRAS, and VAM) in assessing the effect of ASR on the integrity of medium-sized concrete slab that are exposed to the accelerated aging conditions in a laboratory setting. A series of experiments were conducted at Vanderbilt University to collect sufficient degradation data and data analyses were performed. In addition, this report discusses thermography assessment of three bricks cured under different conditions to accelerate ASR-related degradation was also performed. The application of the DIC technique to study ASR-related degradation on a large concrete sample at the University of Tennessee Knoxville was also performed. The main outcomes of NDE techniques and data analytics include:

1. Mechanical deformation technique using steel pegs was used to measure changes in the dimensions of the specimens. Year long measurement showed no signs of mechanical deformation in medium-sized concrete slab.
2. NIRAS successfully detected the damage in the medium-sized concrete slab. The shift in the resonant frequency of the slab was clearly identified. However, NIRAS provides no means to localize the ASR-induced degradation in concrete specimens, irrespective of size of the samples.
3. VAM successfully detected the damage in the medium-sized concrete slab. The above results summarize the experimental work conducted with respected to localization of the damage. Results so far show that the occurrence of sidebands is dependent on the pump and probe location, amplitude, and frequency. Through tuning of the experimental variables, the number of locations where the sidebands were detected can be narrowed by exciting the structure in only certain areas.
4. Thermography data analyses were performed for bricks and medium-sized concrete slab. For bricks, ASR-induced temperature changes measured by the IR thermographic method is able to detect some changes in temperature. For medium-sized concrete slab, ASR-induced temperature changes measured by the IR thermographic method is insignificant. Thus this method sensitivity is not enough for detecting impact of ASR progression on material thermal conductivity for medium-sized concrete slab due to the longer time to heat it.
5. DIC was conducted on the large concrete slab at University of Tennessee, Knoxville. The average value increased to approximately 1250 μm/m in October 2016, and to approximately 2250 μm/m in February 2017. These results indicate that the large concrete slab experienced significant expansion during the period from August 2016 to February 2017.

Future work will focus on the following tasks:

1. VAM technique has shown promise and will investigate the combination of computational modeling with experiments to further improve the damage localization. During the next phase of research, the vibro-acoustic technique will be further studied for detection and localization of ASR in a reinforced-concrete slab and concrete slabs cured at University of Alabama with different reactive aggregates. The uncertainty quantification approaches and integration framework will be advanced further to handle large amounts of observation data. The resulting comprehensive approach will facilitate development of a quantitative, risk-informed framework that would be generalizable for a variety of concrete structures.
2. Destructive evaluation of the medium-sized concrete slab at Vanderbilt University will be performed after all the acoustic data is collected to validate the findings of VAM in localizing the ASR-induced degradation.
3. Continue to monitor the large concrete slab at University of Tennessee, Knoxville using the DIC technique and evaluate if any mechanical deformation can be detected.

4. Investigators will be working on a journal article summarizing the research progress and research findings to date.

6. REFERENCES

Agarwal, V. and S. Mahadevan, 2014, "Concrete Structural Health Monitoring in Nuclear Power Plants," *Office of Nuclear Energy Sensors and Instrumentation Newsletter*, September 2014.

ASTM C1293-08b, 2015, "Standard Test Method for Determination of Length Change of Concrete due to Alkali-Silica Reaction," ASTM International, August 2015.

ASTM C1567-13, 2013, "Standard Test Method for Determining the Potential Alkali-Silica Reactivity of Combinations of Cementitious Materials and Aggregate (Accelerated Mortar-Bar Method)," ASTM International, 2013.

Bruck, P., T. Esselman, and M. Fallin, 2012, "Digital Image Correlation for Nuclear," *Nuclear Engineering International*, April 23, 2012.

Chen, J., A. R. Jayapalan, J.-Y. Kim, K. E. Kurtis, and L. J. Jacobs, 2009, "Nonlinear wave modulation spectroscopy method for ultra-accelerated alkali-silica reaction assessment," *ACI Materials Journal*, Vol. 106, pp. 340–348.

Chen, X. J., J.-Y. Kim, K. E. Kurtis, J. Qu, C. W. Shen, and L. J. Jacobs, 2008, "Characterization of progressive microcracking in Portland cement mortar using nonlinear ultrasonics," *NDT&E International*, Vol. 41, pp. 112–118.

Christensen, J. A., 1990, "NPAR Approach to Controlling Aging in Nuclear Power Plants," *Proceedings of the 17th Water Reactor Safety Information Meeting*, Washington, D.C., NUREG/CP-0105, Vol. 3, pp. 509–529.

Kim, S., D. E. Adams, H., Sohn, G. Rodriguez-Rivera, N. Myrent, R. Bond, J. Vitek, S. Carr, A. Grama, and J. J. Meyer, 2014, "Crack detection technique for operating wind turbine blades using Vibro-Acoustic Modulation," *Structural Health Monitoring*, Vol. 13, No. 6, pp. 660–670.

Kobayashi, K. and N. Banthia, 2011, "Corrosion detection in reinforced concrete using induction heating and infrared thermography," *Journal of Civil Structural Health Monitoring*, Vol. 1, No. 2, pp. 25–35.

Kreitman, K., 2011, "Nondestructive Evaluation of Reinforced Concrete Structures Affected by Alkali-Silica Reaction and Delayed Ettringite Formation," M.S. Thesis: University of Texas at Austin, Austin, Texas.

Lesnicki, K. J., J.-Y. Kim, K. E. Kurtis, and L. J. Jacobs, 2012, "Assessment of alkali-silica reaction damage through quantification of concrete nonlinearity," *Materials and Structures*, Vol. 46, pp. 497–509.

Lesnicki, K. J., J.-Y. Kim, K. E. Kurtis, and L. J. Jacobs, 2014, "Characterization of ASR Damage in Concrete Using Nonlinear Impact Resonance Acoustic Spectroscopy Technique," *NDT&E International*, Vol. 44, No. 8, pp. 721–727.

Mahadevan, S., V. Agarwal, K. Neal, D. Kosson, and D. Adams, 2014, *Interim Report on Concrete Degradation Mechanisms and Online Monitoring Techniques*, INL/EXT-14-33134, Idaho National Laboratory, September 2014.

Mahadevan, S., V. Agarwal, K. Neal, P. Nath, Y. Bao, G. Cai, P. Orme, D. Adams, and D. Kosson, 2016, *A Demonstration of Concrete Structural Health Monitoring Framework for Degradation due to Alkali-Silica Reaction*, INL/EXT-16-38602, Idaho National Laboratory, April 2016.

Naus, D., 2007, "Activities in Support of Continuing the Service of Nuclear Power Plant Safety-Related Concrete Structures," in *Infrastructure Systems for Nuclear Energy,* T. T. C. Hsu, C.-L. Wu, and J.-L. Li (eds), Chichester, United Kingdom: John Wiley & Sons, Ltd.

Neal, K., S. Mahadevan, V. Agarwal, G. Thorne, D. Koester, and B. T. Pham, 2016, *Digital Image Correlation of Concrete Slab at Unievrsity of Tennessee, Knoxville*, INL/EXT-16-39921, Idaho National Laboratory, September 2016.

NextEra Energy Seabrook, 2012, "Impact of Alkali-Silica Reaction on Concrete Structures and Attachments," the Response to Confirmatory Action Letter, SBK-L-12106, from NextEra Energy Seabrook to the Nuclear Regulatory Commission (NRC), May 24, 2012.

Renshaw, J., N. Muthu, and M. Guimaraes, 2014, "Thermographic Inspection of Concrete, Tanks, and Containment Liners," *EPRI Conference,* Charlotte, North Carolina, May 8, 2014.

Ulm, F. J., O. Coussy, L. Kefei, and C. Larive, 2000, "Thermo-chemo-mechanics of ASR expansion in concrete structures," *Journal of Engineering Mechanics*, Vol. 126, No. 3, pp. 233–242.

Vehorn, K. A., 2013, "Vibro-Acoustic Modulation as a Baseline-Free Structural Health Monitoring Technique," M.S. Thesis, University of Dayton, Dayton, Ohio, https://etd.ohiolink.edu/rws_etd/document/get/dayton1374508274/inline.